IMMUNE CHECKPOINTS

Functional differences between rodent and human PD-1 linked to evolutionary divergence

Takeya Masubuchi[1], Lin Chen[2]†, Nimi Marcel[3]†, George A. Wen[1]†, Christine Caron[4], Jibin Zhang[1], Yunlong Zhao[1], Gerald P. Morris[4], Xu Chen[5], Stephen M. Hedrick[3], Li-Fan Lu[3], Chuan Wu[6], Zhengting Zou[2]*, Jack D. Bui[4]*, Enfu Hui[1]*

Mechanistic understanding of the inhibitory immunoreceptor PD-1 is largely based on mouse models, but human and mouse PD-1 share only 59.6% amino acid identity. Here, we found that human PD-1 is more inhibitory than mouse PD-1, owing to stronger interactions with the ligands PD-L1 and PD-L2 and more efficient recruitment of the effector phosphatase Shp2. In a mouse melanoma model with adoptively transferred T cells, humanization of a PD-1 intracellular domain disrupted the antitumor activity of CD8$^+$ T cells and increased the magnitude of anti–PD-1 response. We identified a motif highly conserved across vertebrate PD-1 orthologs, absent in rodents, as a key determinant for differential Shp2 recruitment. Evolutionary analysis suggested that PD-1 underwent a rodent lineage–specific functional attenuation during evolution. Together, our study uncovers species-specific features of the PD-1 pathway, with implications for PD-1 evolution and differential anti–PD-(L)1 responses in mouse models and human patients.

INTRODUCTION

Studies in laboratory mice have offered valuable insights into the molecular and cellular mechanisms of immune function. In this regard, mouse models have been pivotal in translational studies, including identifying immune checkpoint inhibitors for cancer immunotherapy (*1*–*6*). Nevertheless, mice and humans differ considerably in the relative abundance of immune cell types, gene expression patterns, and the specific gene functions (*7*–*9*). These differences may explain why checkpoint inhibitor studies in mice have not yet offered substantial insight into the limitations and adverse reactions of immune therapy in human patients (*10*–*14*). An in-depth understanding of the conservation and divergence of mouse and human immunity at the molecular level is required to better translate findings from mouse models to human trials.

The immune checkpoint receptor programmed cell death protein 1 (PD-1) regulates peripheral tolerance and immunity against cancer and infection (*1*–*5*, *15*–*18*). Whereas PD-1–blocking drugs have demonstrated impressive antitumor activity in some patients with cancer (*3*, *19*–*23*), the low response rates and associated immune-related adverse effects, which are often not mirrored in mice, necessitate a better understanding of PD-1 signaling in a human-specific context.

Best known to be expressed by T cells, PD-1 has an immunoglobulin-variable-like (IgV) ectodomain (ECD), a transmembrane domain (TMD), and an intracellular domain (ICD) containing two conserved phosphorylatable tyrosines embedded in an immunoreceptor tyrosine inhibitory motif (ITIM) and an immunoreceptor tyrosine switching motif (ITSM), respectively. Programmed death ligand 1 (PD-L1), the major ligand of PD-1, has an N-terminal IgV domain that binds to the IgV of PD-1 through the front β-face (GFCC′) (*24*–*26*). This binding triggers PD-1 phosphorylation at ITIM and ITSM, which recruits the phosphatase Shp2 to dephosphorylate components in the TCR and costimulatory signaling pathways (*27*–*30*).

One remarkable yet largely overlooked feature of PD-1 is its relatively low conservation across vertebrates. Whereas intracellular enzymes such as Lck, Zap70, Csk, and Shp2 exhibit 95 to 99% amino acid sequence identity between humans and mice, human PD-1 (*hu*PD-1) and mouse PD-1 (*mo*PD-1) share only 59.6% amino acid sequence identity, exhibiting substantial differences in their ECDs, TMDs, and ICDs. Likewise, many other inhibitory immunoreceptors, including BTLA, Tim3, Lag3, TIGIT, SIRPα, and Siglecs, exhibit low sequence identity between humans and mice, except for cytotoxic T-lymphocyte associated protein 4 (CTLA-4), whose ICD is 100% conserved. The cross-species divergence in PD-1 sequence suggests that it is still being refined by evolutionary pressures (*31*), but little is known about why, how, and to what extent PD-1 function differs across species.

Here, we quantitatively compared the inhibitory activities of *hu*PD-1, *mo*PD-1, and their chimeras using biophysical assays, coculture assays, and mouse tumor models. These experiments revealed substantial divergence between *hu*PD-1 and *mo*PD-1 at both the biochemical and functional levels. We found that rodent PD-1 has a special pre-ITSM sequence that confers its weaker Shp2 recruitment and less inhibitory function as a result of a gradual functional attenuation due to relaxation of natural selection throughout evolution. These results demonstrate cross-species differences in the PD-1:PD-L1 pathway with implications for the translation of preclinical findings related to human therapeutics.

RESULTS

*Hu*PD-1 is more inhibitory than *mo*PD-1 in both human and mouse T cells

Quantitative comparison of *hu*PD-1 and *mo*PD-1 activity requires precise control of their expression levels in the same cellular background. We first sought to achieve this in a well-defined coculture system, using

[1]Department of Cell and Developmental Biology, School of Biological Sciences, University of California San Diego, La Jolla, CA 92093, USA. [2]Key Laboratory of Zoological Systematics and Evolution, Institute of Zoology, Chinese Academy of Sciences, Beijing 100101, China. [3]Department of Molecular Biology, School of Biological Sciences, University of California San Diego, La Jolla, CA 92093, USA. [4]Department of Pathology, University of California San Diego, La Jolla, CA 92093, USA. [5]Department of Neurosciences, University of California San Diego, La Jolla, CA 92093, USA. [6]Experimental Immunology Branch, National Cancer Institute, National Institutes of Health, Bethesda, MD 20892, USA.
*Corresponding author. Email: zouzhengting@ioz.ac.cn (Z.Z.); jbui@ucsd.edu (J.D.B.); enfuhui@ucsd.edu (E.H.)
†These authors contributed equally to this work.

Jurkat human T cell line (Jurkat) as the responder and Raji human B cell line (Raji) as the antigen-presenting cell (APC). We established PD-1–deficient (*PDCD1*$^{-/-}$) Jurkat cells via CRISPR-Cas9 and transduced them with either *hu*PD-1 or *mo*PD-1 (Fig. 1A), each tagged with a C-terminal monomeric GFP (mGFP). This allowed us to assess the expression of both PD-1 orthologs using a common fluorescent readout, rather than using antibody staining that would require two clones of anti–PD-1. Optimization of lentivirus titers allowed us to establish two Jurkat lines stably expressing similar levels of either *hu*PD-1–mGFP or *mo*PD-1–mGFP (Fig. 1A). The use of the weak dSV40 promoter ensured modest PD-1 expression resembling endogenous PD-1 levels on human primary CD4$^+$ T cells (fig. S1). To establish PD-L1–expressing APCs, we transduced CD80-deficient (*CD80*$^{-/-}$) Raji cells with either *hu*PD-L1–mCherry or *mo*PD-L1–mCherry, expressed at comparable amounts as indicated by mCherry fluorescence (Fig. 1A). CD80 deletion avoided *cis*-CD80:PD-L1 interaction, known to block PD-1:PD-L1 interaction (*32*–*35*).

To compare the suppressive activities of *hu*PD-1 and *mo*PD-1, we performed two parallel coculture assays with matched species of PD-1 and PD-L1: (i) Jurkat (*hu*PD-1–mGFP) incubated with superantigen staphylococcal enterotoxin E (SEE)–loaded Raji cells (*hu*PD-L1–mCherry) to examine *hu*PD-1:PD-L1 signaling; (ii) Jurkat (*mo*PD-1–mGFP) incubated with SEE-loaded Raji cells (*mo*PD-L1–mCherry) to recapitulate *mo*PD-1:PD-L1 signaling. In both assays, we titrated PD-1:PD-L1 interactions using atezolizumab, an anti–PD-L1 antibody that blocks both *hu*PD-L1 and *mo*PD-L1 with similar capacities (*36*). Atezolizumab dose-dependently increased interleukin-12 (IL-2) production in both settings (Fig. 1B). These data revealed that *hu*PD-1:PD-L1 interaction inhibited IL-2 secretion by ~60%, whereas the mouse counterpart did so by only ~31%. Titration of SEE revealed that *hu*PD-1:PD-L1 was consistently more suppressive than *mo*PD-1:PD-L1 across varying TCR signaling strengths (Fig. 1C), despite the slightly lower expression of *hu*PD-L1 than *mo*PD-L1 (Fig. 1A). Although Shp2, a known mediator of PD-1 signaling, is highly conserved between humans and mice (fig. S2), we considered that the human-derived Jurkat environment might be less permissive to *mo*PD-1, thereby mitigating its inhibitory activity. We therefore performed a complementary experiment using DO11.10 mouse T cell hybridoma (DO11.10 cells) cocultured with A20 mouse B cell lines (A20 cells), which present ovalbumin (OVA)–derived peptide 323 to 339 ($OVA_{323-339}$) via class II major histocompatibility complex (MHC-II) I-A^d (Fig. 1D). We transduced *Pdcd1*$^{-/-}$*Cd274*$^{-/-}$ DO11.10 cells with *hu*PD-1–mGFP or *mo*PD-1–mGFP and transduced *Cd274*$^{-/-}$*Cd80*$^{-/-}$*Cd86*$^{+/+}$ A20 cells with *hu*PD-L1–mCherry or *mo*PD-L1–mCherry. Using fluorescence activated cell sorting (FACS), we obtained two DO11.10 lines expressing similar levels of *hu*PD-1–mGFP and *mo*PD-1–mGFP and two A20 lines expressing comparable amounts of *hu*PD-L1–mCherry and *mo*PD-L1–mCherry (Fig. 1D and fig. S3, A and B). Coculture assays showed that, even in the mouse-derived DO11.10 and A20 cells, *hu*PD-1:PD-L1 interaction was more suppressive than *mo*PD-1:PD-L1 interaction (Fig. 1E). Collectively, when stimulated by comparable amounts of cognate PD-L1, *hu*PD-1 is more inhibitory than *mo*PD-1 in T cells of both human and mouse origin.

Both ECD and ICD contribute to the stronger inhibitory function of *huPD-1*

*Hu*PD-1 and *mo*PD-1 share 61.2%, 33.3%, and 58.0% amino acid identities in the ECD, TMD, and ICD, respectively. We next determined which domain(s) of PD-1 underlie(s) the different inhibitory activities of *hu*PD-1 and *mo*PD-1 using PD-1 chimeras. We created Jurkat cell lines expressing similar levels of *hu*PD-1, *mo*PD-1, or chimeric PD-1 in which the ECD, TMD, or ICD of *hu*PD-1 was swapped with the corresponding domain of *mo*PD-1, designated as *hu*PD-1^{moECD}, *hu*PD-1^{moTMD}, and *hu*PD-1^{moICD}, respectively (Fig. 2A). We then cocultured each Jurkat cell line with SEE-pulsed *CD80*$^{-/-}$*CD86*$^{+/+}$ Raji cells expressing either *hu*PD-L1–mCherry or *mo*PD-L1–mCherry to ensure matched species of PD-L1 and the ECD species of PD-1 chimera. These experiments showed that swapping either the ECD or the ICD, but not the TMD, decreased the abilities of *hu*PD-1 to inhibit both IL-2 secretion and CD69 expression (Fig. 2B). These results suggest that both the ECD and the ICD contribute to the more suppressive activity of *hu*PD-1.

In a reciprocal experiment, we compared the inhibitory activity of PD-1 chimeras in the DO11.10:A20 mouse cell culture system, using *mo*PD-1 as the template to construct three chimeras: *mo*PD-1^{huECD}, *mo*PD-1^{huTMD}, and *mo*PD-1^{huICD}, with either the ECD, TMD, or ICD of *mo*PD-1 replaced by the corresponding domain of *hu*PD-1. We generated five DO11.10 cell lines expressing comparable amounts of

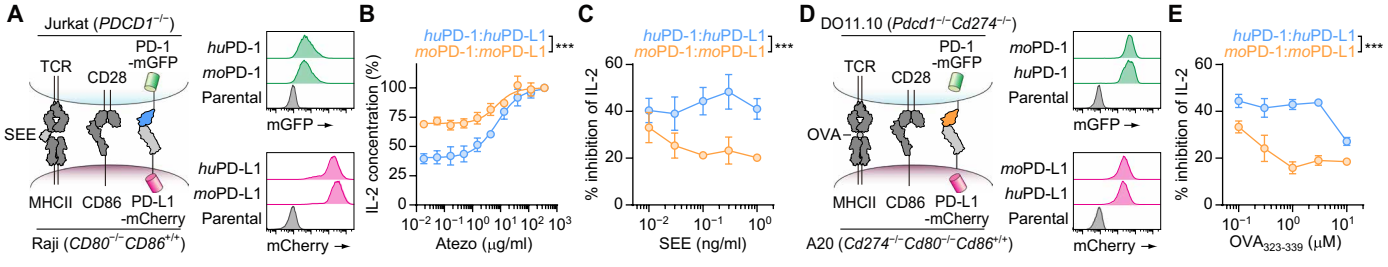

Fig. 1. *Hu*PD-1:PD-L1 interaction more potently inhibited T cell function than *mo*PD-1:PD-L1 interaction. (**A**) Left: Cartoon depicting a human-derived coculture assay containing Jurkat expressing TCR, CD28, and mGFP-tagged *hu*PD-1 or *mo*PD-1 and SEE–pulsed Raji APCs expressing MHC-II, CD86, and mCherry-tagged *hu*PD-L1 or *mo*PD-L1. Right: FACS histograms showing the expression of the indicated PD-1–mGFP or PD-L1–mCherry variant on the Jurkat or Raji cells. (**B**) Atezolizumab dose responses of secreted IL-2 in the indicated Jurkat:Raji coculture in the presence of SEE (0.1 ng/ml). Data were normalized to the IL-2 amounts at the highest concentration of atezolizumab. (**C**) SEE dose responses of % IL-2 inhibition mediated by either the *hu*PD-1:*hu*PD-L1 or *mo*PD-1:*mo*PD-L1 pair in the Jurkat:Raji coculture assay depicted in (A). Raji cells were pretreated with atezolizumab (0 or 120 μg/ml). (**D**) Left: Cartoon depicting a mouse-derived coculture assay containing DO11.10 cells expressing TCR, CD28, and mGFP-tagged *hu*PD-1 or *mo*PD-1 and $OVA_{323-339}$–pulsed A20 APCs expressing MHC-II, CD86, and mCherry-tagged *hu*PD-L1 or *mo*PD-L1. Right: FACS histograms showing the expression of the indicated PD-1–mGFP or PD-L1–mCherry variant on the DO11.10 or A20 cell. (**E**) $OVA_{323-339}$ dose responses of % IL-2 inhibition mediated by either the *hu*PD-1:*hu*PD-L1 or *mo*PD-1:*mo*PD-L1 pair in the DO11.10:A20 coculture assay depicted in (D). Data are mean ± SD from three independent technical replicates. ***$P < 0.001$; two-way ANOVA.

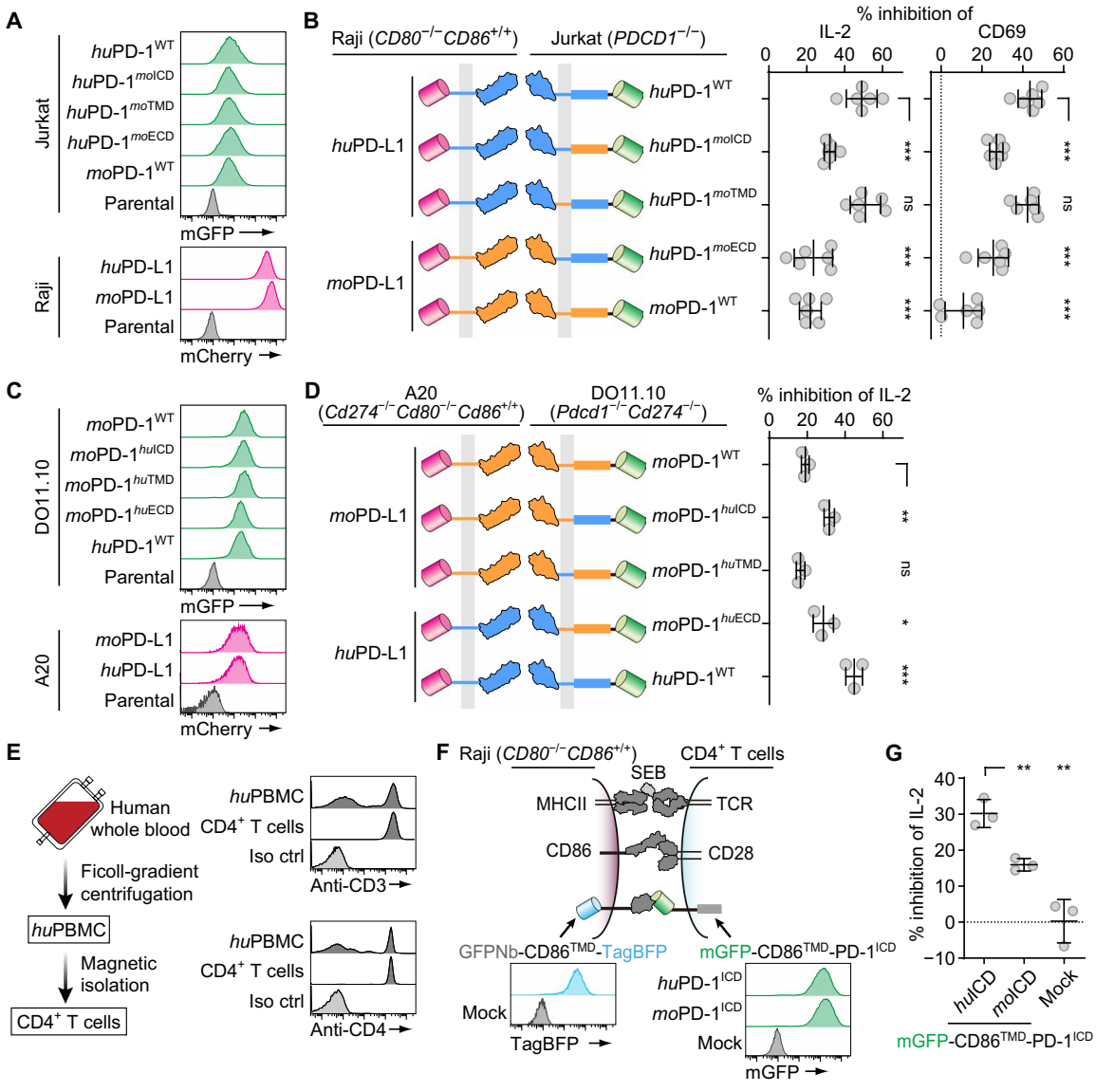

Fig. 2. Both the ECD and ICD of *hu*PD-1 contribute to its stronger inhibitory function than that of *mo*PD-1. (**A**) FACS histograms showing the expressions of indicated mGFP-tagged PD-1 or mCherry-tagged PD-L1 variants on Jurkat or Raji cells used for cocultures. (**B**) Left: A cartoon depicting the PD-1:PD-L1 pairs tested in five parallel Jurkat:Raji coculture assays. Right: Bar graphs showing the % inhibition of IL-2 secretion and of CD69 expression by the PD-1:PD-L1 pairs indicated on the left ($n = 6$ independent technical replicates). (**C**) FACS histograms showing the expression of the indicated mGFP-tagged PD-1 or mCherry-tagged PD-L1 variants on DO11.10 or A20 cells used for cocultures. (**D**) Left, a cartoon depicting the PD-1:PD-L1 pairs tested in five parallel A20:DO11.10 coculture assays. Right: A bar graph showing the % inhibition of IL-2 secretion by the PD-1:PD-L1 pairs indicated on the left ($n = 3$ independent technical replicates). (**E**) Left: Diagram showing the purification method for human primary $CD4^+$ T cells. Right: FACS histograms of CD3 and CD4 expression on *hu*PBMCs and $CD4^+$ T cells. (**F**) Top: cartoon depicting a coculture assay containing $CD4^+$ T cells expressing TCR, CD28, and $mGFP^{ECD}$–TMD–$PD\text{-}1^{ICD}$, and SEB-pulsed Raji APCs expressing MHC-II, CD86, and GFPNb-TMD-TagBFP. Bottom: FACS histograms showing the expression of indicated PD-1 chimera or GFPNb-TM-TagBFP on $CD4^+$ T or Raji cells, respectively. (**G**) A dot plot showing % inhibition of IL-2 secretion by the PD-1 chimera:GFPNb association in the $CD4^+$ T cell:Raji coculture depicted in (F) ($n = 3$ independent technical replicates). Data are mean ± SD based on the sample numbers indicated in each panel. $^*P < 0.05$; $^{**}P < 0.01$; $^{***}P < 0.001$; ns, not significant; Student's *t* test.

mGFP-tagged *hu*PD-1, *mo*PD-1, or each of the three PD-1 chimeras (Fig. 2C) and stimulated each with peptide-pulsed A20 cells expressing PD-L1 whose species matched the ECD of the corresponding PD-1 variant. Consistent with the results in the Jurkat:Raji system, both the ECD and ICD contributed to the stronger activity of the human orthologs (Fig. 2D).

To validate the differential inhibitory capacities of *hu*PD-1 and *mo*PD-1 in primary T cells, we transduced human $CD4^+$ T cells with either *hu*PD-1 or *mo*PD-1, each with the ECD replaced by mGFP, and expressed at similar levels (Fig. 2, E and F). To trigger GFP–PD-1 chimeras without stimulating endogenous PD-1, we created $CD80^{-/-}CD86^{+/+}$ Raji APCs expressing a GFPNb-TMD-tagBFP, in which a GFP nanobody was fused to CD86TMD and a C-terminal tagBFP. Upon coculturing GFP^+CD4^+ T cells with SEB-pulsed $CD80^{-/-}CD86^{+/+}GFPNb\text{-}TMD\text{-}tagBFP^+$ Raji APCs (Fig. 2F), GFP^{ECD}–*hu*PD-1^{ICD} and GFP^{ECD}–*mo*PD-1^{ICD} inhibited IL-2 production by 30

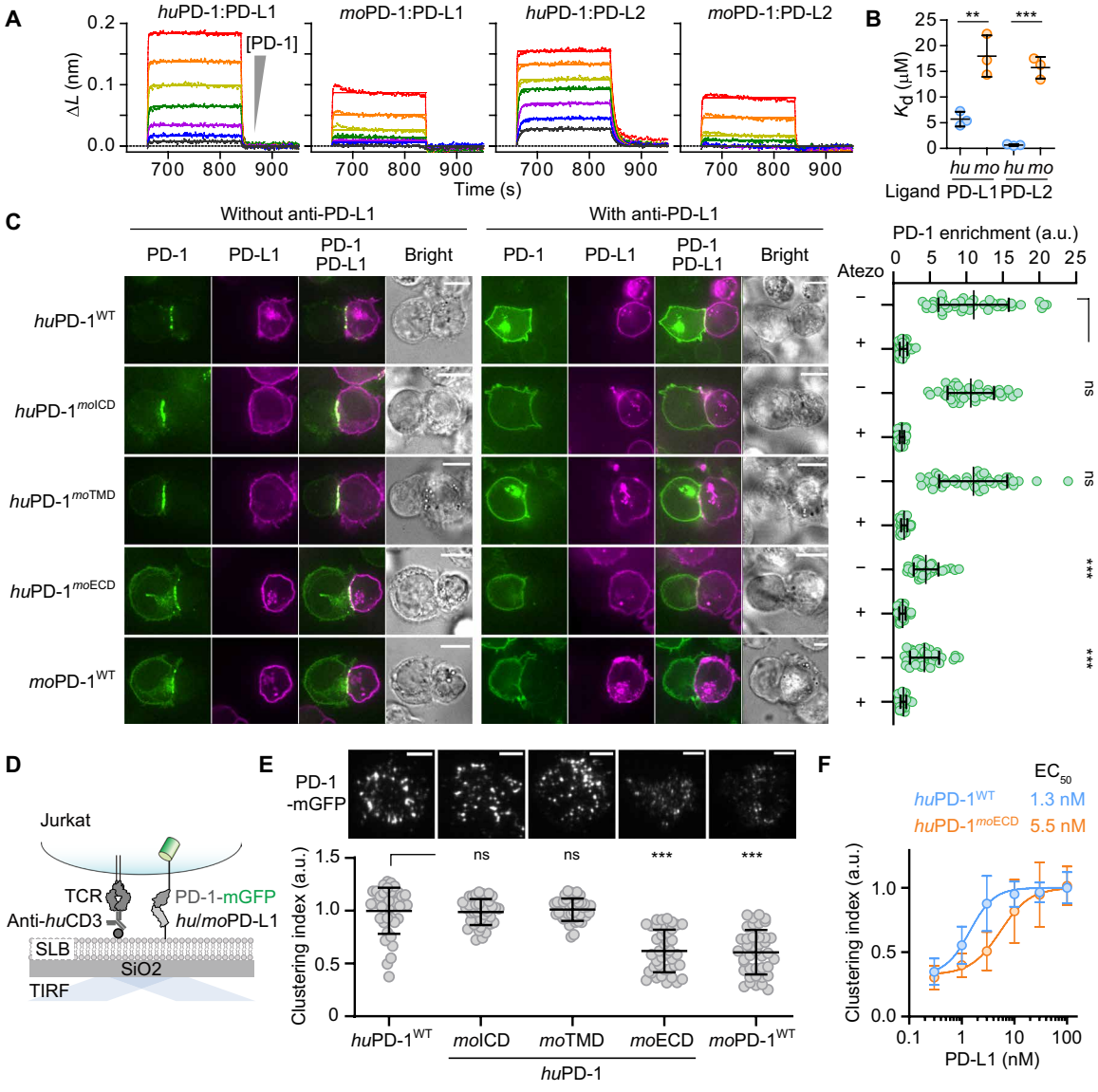

Fig. 3. Human PD-1 ECD associates with its ligands more strongly than mouse PD-1 ECD. (**A**) Representative BLI data obtained for the indicated PD-1:ligand pairs with the PD-L1 or PD-L2 immobilized on the sensor chip and increasing concentrations of PD-1–ECD presented in the solution. (**B**) K_d values of the indicated PD-1:ligand pairs based on the BLI experiments ($n = 3$ independent technical replicates). (**C**) Left: Representative confocal images of a conjugate between Jurkat expressing the indicated PD-1 variants (green) and Raji cells expressing the indicated PD-L1 variants (magenta) with or without anti–PD-L1 (atezolizumab). Right: A dot plot showing the synaptic enrichment score of each PD-1 variant in the presence or absence of atezolizumab ($n = 40$ cells). (**D**) A cartoon depicting a cell-SLB assay, in which Jurkat cells expressing the mGFP-tagged PD-1 variant interacted with a SLB functionalized with anti-*hu*CD3ε and *hu*/*mo*PD-L1–His. PD-1 microclusters were visualized via TIRF-M. (**E**) Top: Representative TIRF images showing microclusters of the indicated mGFP-tagged PD-1 variant in a Jurkat cell that contacted the SLB functionalized with 3 nM *hu*PD-L1 or *mo*PD-L1 that matched the species of the ECD of the corresponding PD-1 variant. Bottom: Dot plots showing the clustering indices of all five PD-1 variants (see Materials and Methods) ($n = 40$ cells). (**F**) Dose-response curves showing PD-1 clustering indices of the indicated PD-1 variant plotted against the concentration of PD-L1 ($n = 3$ independent technical replicates). Scale bars, 5 μm. Data are mean ± SD based on the sample numbers indicated in each panel. $^{**}P < 0.01$; $^{***}P < 0.001$; ns, not significant; Student's *t* test.

and 16%, respectively, compared with conditions using *CD80*$^{-/-}$*CD86*$^{+/+}$ Raji APCs lacking GFPNb-TMD-tagBFP (Fig. 2G). This result further supported the notion that *hu*PD-1 ICD is intrinsically more suppressive than *mo*PD-1 ICD.

*Hu*PD-1:PD-L1/2 interaction is stronger than *mo*PD-1:PD-L1/2 interaction

Having shown that the stronger inhibitory activity of *hu*PD-1 mapped in part to the ECD (Fig. 2, *hu*PD-1^{WT} versus *hu*PD-1^{moECD}, *mo*PD-1^{huECD} versus *mo*PD-1^{WT}), we next compared the three-dimensional (3D) affinities of *hu*PD-1 and *mo*PD-1 with their cognate ligands using biolayer interferometry (BLI). *hu*PD-1^{ECD} or *mo*PD-1^{ECD} dose-dependently bound sensor-immobilized, species-matched PD-L1^{ECD} or PD-L2^{ECD} (Fig. 3A). The resulting dissociation constants (K_d) showed a 3.2-fold higher affinity for the human PD-1:PD-L1 interaction and a 24-fold higher affinity for the human PD-1:PD-L2 interaction compared with their mouse counterparts (Fig. 3B). These results are in qualitative agreement with surface

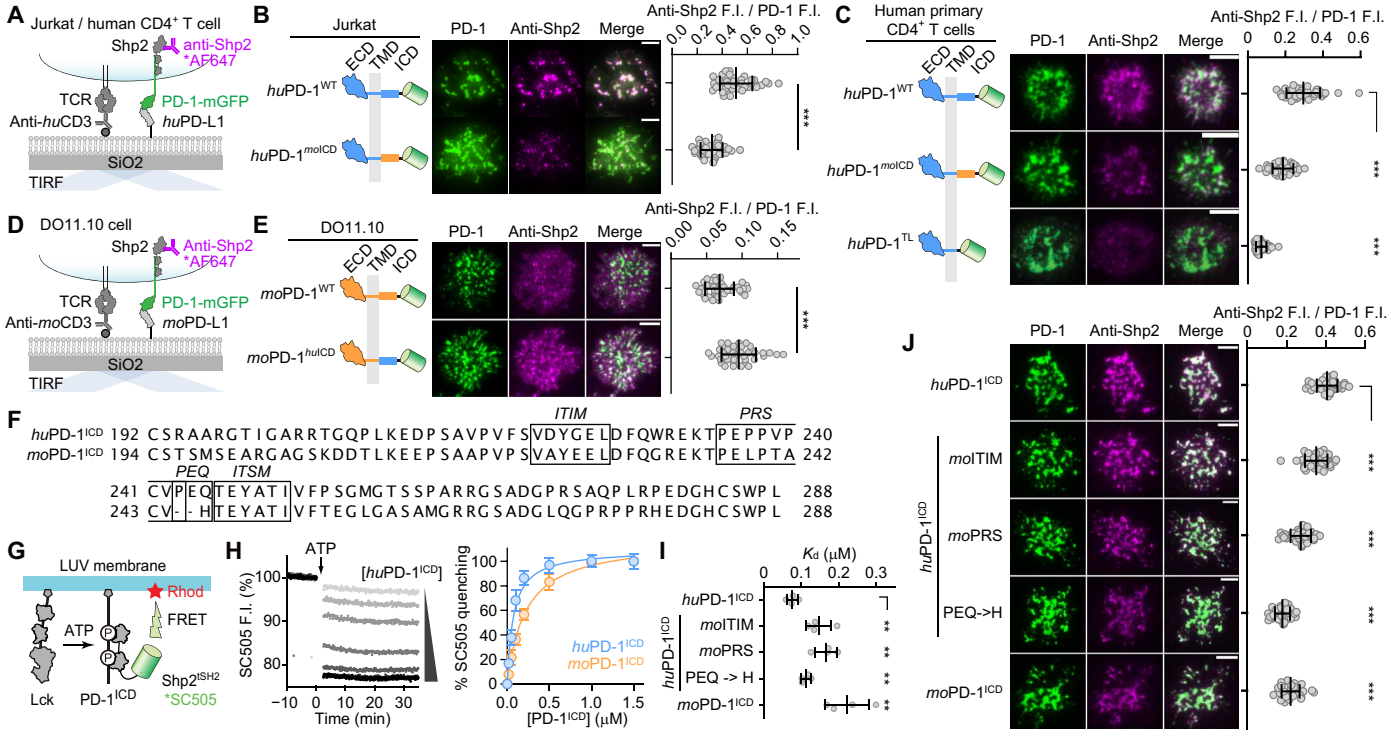

Fig. 4. *Hu*PD-1 more strongly recruits Shp2 than does *mo*PD-1 because of three nonconserved motifs. (**A**) A cartoon showing a cell-SLB assay for TIRF imaging of PD-1:Shp2 association in Jurkat or human CD4$^+$ T cells. (**B**) Left: Representative TIRF images of the indicated mGFP-tagged PD-1 variants (green) and anti-Shp2 (magenta) at the interface of a Jurkat cell and the SLB as depicted in (A). Right: Dot plots showing the anti-Shp2 F.I. normalized to PD-1 F.I. ($n = 40$ cells). (**C**) Same as (B), except that human CD4$^+$ T cells expressing the indicated PD-1 variants were imaged ($n = 40$ cells). (**D** and **E**) Same as (A) and (B), except that DO11.10 cells were observed. (**F**) Amino acid sequence alignment of *hu*PD-1^{ICD} and *mo*PD-1^{ICD}, with ITIM, PRS, PEQ/H, and ITSM highlighted. (**G**) Cartoon of a liposome reconstitution assay for measuring PD-1^{ICD}:Shp2^{tSH2} interaction. (**H**) Left: Representative time courses of SC505 (Shp2^{tSH2}) F.I. at increasing concentrations of *hu*PD-1^{ICD}. Right: % SC505 quenching 30 min after ATP addition plotted against the concentrations of *hu*PD-1^{ICD} and *mo*PD-1^{ICD} ($n = 3$ independent technical replicates). (**I**) Bar graphs summarizing apparent K_d of Shp2^{tSH2} interaction with indicated PD-1^{ICD} variants determined via assays shown in (G) and (H) ($n = 3$ independent technical replicates). (**J**) Left: Representative TIRF images showing Shp2 recruitment to microclusters of indicated PD-1 variants in a Jurkat-SLB assay. Right: Dot plots showing anti-Shp2 F.I. normalized to PD-1 F.I. ($n = 40$ cells). Scale bars, 5 μm. Data are mean ± SD based on the sample numbers indicated in each panel. $^{**}P < 0.01$; $^{***}P < 0.001$; ns, not significant; Student's *t* test.

plasmon resonance measurements using refolded bacterially expressed proteins (*37*). Moreover, in a cell-free membrane reconstitution assay (*34*, *38*), *hu*PD-1:*hu*PD-L1 interactions drove more association of large unilamellar vesicles (LUVs) with supported lipid bilayers (SLBs) than *mo*PD-L1:*mo*PD-1 interactions (fig. S4), indicating a higher 2D affinity for the human pair.

We further compared human and mouse PD-1:PD-L1 interactions using full-length *hu*PD-1, *mo*PD-1, and their chimeras. To examine PD-1:PD-L1 trans-interactions (*34*, *38*), we measured PD-L1–dependent PD-1 enrichment at the APC:T cell interface in a Jurkat:Raji coculture assay. After incubation of Jurkat cells expressing mGFP-tagged *hu*PD-1, *mo*PD-1, or their chimeras with SEE-loaded Raji APCs (*CD80*$^{-/-}$*CD86*$^{+/+}$) expressing either *hu*PD-L1–mCherry or *mo*PD-L1–mCherry, we observed more accumulation of PD-1 variants with the human ECD (*hu*PD-1^{WT}, *hu*PD-1^{moTMD}, and *hu*PD-1^{moICD}) to the Jurkat:Raji border compared with PD-1 variants containing the mouse ECD (*hu*PD-1^{moECD} and *mo*PD-1^{WT}) (Fig. 3C). As expected, the presence of atezolizumab abrogated the synaptic enrichment of PD-1 (Fig. 3C). We extended these findings in a PD-1 microcluster assay (*27*) that uses SLBs as artificial APCs (Fig. 3D). When the aforementioned Jurkat cells landed onto SLBs containing Okt3 (anti-*hu*CD3ε), human ICAM1 (*hu*ICAM1), and equal amounts of *hu*PD-L1 or *mo*PD-L1, PD-1 variants containing *hu*PD-1 ECD (*hu*PD-1^{WT}, *hu*PD-1^{moTMD}, and *hu*PD-1^{moICD}) formed more intense microclusters than PD-1 variants containing mouse ECD (*hu*PD-1^{moECD} and *mo*PD-1^{WT}), recorded by total internal reflection fluorescence microscopy (TIRF-M) (Fig. 3E, fig. S5, and movies S1 and S2). Titration of PD-L1 on SLB revealed that *hu*PD-1^{moECD} required 4.2-fold more cognate ligand to cluster to a similar degree as did *hu*PD-1^{WT} (Fig. 3F). Collectively, data in this section demonstrate that *hu*PD-1 binds cognate PD-L1 and PD-L2 more strongly than *mo*PD-1.

*Hu*PD-1 recruits Shp2 more strongly than *mo*PD-1

We then turned our attention to the ICD, because our chimera experiments indicated that the *hu*PD-1 ICD mediates stronger inhibitory effects than the *mo*PD-1 ICD (Fig. 2, *hu*PD-1^{WT} versus *hu*PD-1^{moICD} and *mo*PD-1^{huICD} versus *mo*PD-1^{WT}). The ICD of PD-1 is known to recruit Shp2 (*27*, *39*). Treatment of T cell:APC cocultures with SHP099, an allosteric inhibitor of Shp2 (*40*), decreased the ability of PD-1 to inhibit IL-2 production by about 50% in both human and mouse CD8$^+$ T cells (fig. S6). To determine the biochemical mechanism underlying the differential suppressive activities of *hu*PD-1 ICD and *mo*PD-1 ICD, we compared their abilities to recruit Shp2 by imaging PD-1:Shp2 association in T cells in a cell-SLB system (Fig. 4A). After incubating Jurkat cells expressing *hu*PD-1^{WT}–mGFP or *hu*PD-1^{moICD}–mGFP with *hu*PD-L1–functionalized SLBs, we fixed

and permeabilized the SLB-associated cells and stained endogenous Shp2 with Alexa Fluor 647 anti-Shp2 (anti-Shp2*AF647) (Fig. 4A). TIRF-M detected intense microclusters for both *hu*PD-1^{WT}–mGFP and *hu*PD-1^{moICD}–mGFP, given that they both contained the ECD of *hu*PD-1. However, *hu*PD-1^{WT}–mGFP recruited significantly more Shp2 than did *hu*PD-1^{moICD}–mGFP (Fig. 4B). Likewise, when human primary CD4$^+$ T cells transduced with mGFP-tagged *hu*PD-1^{WT}, *hu*PD-1^{moICD}, or tailless *hu*PD-1 (*hu*PD-1^{TL}) contacted SLBs containing anti-*hu*CD3ε, *hu*PD-L1, and *hu*ICAM1, *hu*PD-1^{WT} microclusters recruited more Shp2 than did *hu*PD-1^{moICD} in CD4$^+$ T cells, based on either endogenous Shp2 immunostaining or transduced mCherry-Shp2 (Fig. 4C and fig. S7). The dim anti-Shp2 signal detected within *hu*PD-1^{TL} foci was likely due to endogenous PD-1. We further compared the abilities of the *hu*PD-1 ICD and *mo*PD-1 ICD to recruit mouse Shp2 in mouse cells. When DO11.10 cells expressing *mo*PD-1^{WT}-mGFP or *mo*PD-1^{huICD}-mGFP contacted SLBs harboring anti-*mo*CD3ε, *mo*PD-L1, and *mo*ICAM1 (Fig. 4D), both PD-1 variants formed microclusters, but *mo*PD-1^{huICD} recruited more Shp2 than did *mo*PD-1^{WT}, as indicated by anti-Shp2*AF647 staining (Fig. 4E). Notably, Shp2 is highly conserved between human and mouse, especially the PD-1 binding module tandem SH2 domains (tSH2), exhibiting 100% sequence identity between the two species (fig. S2). Thus, *hu*PD-1 is more capable of recruiting the intracellular effector Shp2 than *mo*PD-1.

A pre-ITSM PEQ motif in *hu*PD-1 drives stronger Shp2 recruitment

The stronger Shp2 recruitment by *hu*PD-1 than by *mo*PD-1 was unexpected, because ITSM, the major Shp2 docking site, is identical in *hu*PD-1 and *mo*PD-1. We next sought to identify the molecular determinants in the PD-1 ICD underlying the differential Shp2 recruitment activities of human and mouse orthologs. Despite the conserved ITSM, PD-1 shows variations in the pre-ITSM regions: *hu*PD-1 contains an identifiable proline-rich sequence (PRS) and a Pro-Glu-Gln (PEQ) sequence immediately upstream of ITSM; *mo*PD-1 differs from *hu*PD-1 by two residues in the ITIM and four in the PRS and replaces the PEQ motif with a single His (Fig. 4F). To assess whether these motifs contribute to Shp2 recruitment, we constructed, expressed, and purified His-tagged *hu*PD-1 ICD WT and mutants with each of the three motifs (ITIM, PRS, and PEQ) replaced with the corresponding segment in *mo*PD-1, designated as *hu*PD-1–ICD^{moITIM}, *hu*PD-1–ICD^{moPRS}, and *hu*PD-1–ICD$^{PEQ→H}$, respectively. We then measured the abilities of these proteins to recruit Shp2^{tSH2} using a LUV reconstitution assay with a Förster resonance energy transfer (FRET) readout, as described (Fig. 4G) (*41*). We coupled each of the five His–PD-1 ICD variants together with His-tagged Lck kinase to rhodamine (energy acceptor)–labeled LUVs and presented SNAP-cell-505 (SC505, energy donor)–labeled Shp2^{tSH2} in solution. Subsequent ATP addition triggered PD-1 ICD phosphorylation by Lck and recruitment of Shp2^{tSH2}*SC505, leading to FRET-mediated SC505 quenching by rhodamine (Fig. 4G) in a PD-1 ICD dose–dependent manner, allowing us to calculate the apparent K_d values (Fig. 4H). These experiments revealed a 2.9-fold stronger Shp2 affinity for *hu*PD-1–ICD^{WT} than for *mo*PD-1–ICD^{WT} (76 nM K_d for *hu*PD-1 and 220 nM K_d for *mo*PD-1), consistent with data in cells (Fig. 4, B, C, and E). Likewise, Shp1, reported to mediate PD-1 signaling upon Shp2 deletion (*42*), also bound to *hu*PD-1–ICD^{WT} with a higher affinity than to *mo*PD-1–ICD^{WT} (fig. S8). Swapping the ITIM, PRS, or PEQ of *hu*PD-1 with the corresponding motif in *mo*PD-1 decreased the Shp2 affinity, as reflected by greater K_d values for *hu*PD-1–ICD^{moITIM}, *hu*PD-1–ICD^{moPRS}, and *hu*PD-1–ICD$^{PEQ→H}$ than for *hu*PD-1–ICD^{WT} (Fig. 4I). These results suggest that besides the conserved ITSM, *hu*PD-1:Shp2 interaction is contributed by three nonconserved motifs—ITIM, PRS, and PEQ—that are either weakened or absent in *mo*PD-1.

To validate the results of the LUV-FRET assays in a cellular context, we transduced Jurkat cells with mGFP-tagged *hu*PD-1 variants in which the ITIM, PRS, or PEQ motif was replaced with the corresponding motif in *mo*PD-1 and measured Shp2 recruitment to microclusters of these PD-1 mutants (Fig. 4A). Consistent with the LUV-FRET assay, all three domain-swapping mutants exhibited weaker Shp2 recruitment compared with *hu*PD-1^{WT} (Fig. 4J). The relative magnitude of the effect differed in the LUV-FRET assay and the cellular assay, likely because of the use of a truncated form (tSH2) of Shp2 or the lack of other cellular factors in the LUV-FRET assay. In the cellular assay, PEQ→H mutation produced the largest decrease in Shp2 recruitment, to a similar extent as did *hu*PD-1^{moICD}, which had the entire ICD replaced by the mouse version (Fig. 4J). Altogether, data in this section demonstrated that despite the identical ITSM, *hu*PD-1 is superior to *mo*PD-1 in Shp2 recruitment, largely attributable to the PEQ motif that is substituted by a His in *mo*PD-1.

PD-1–ICD humanization severely impairs mouse T cell antitumor activity

We next determined whether humanization of PD-1 increased its immunosuppressive capacity in a mouse tumor model, using adoptively transferred tumor-specific TCR-transgenic CD8$^+$ T cells expressing either *mo*PD-1 or ICD-humanized PD-1. We isolated *Pdcd1*$^{-/-}$ P14 TCR transgenic CD8$^+$ T cells recognizing H-2D^b (MHC-I)–restricted lymphocytic choriomeningitis virus (LCMV)–derived peptide antigen gp$_{33-41}$. Using a retrovirus encoding an exogenous PD-1 (exoPD-1) and cell surface marker Thy1.1 (Fig. 5A), we reconstituted each of the three exoPD-1 variants: *mo*PD-1^{WT}, *mo*PD-1^{huICD} (whose entire ICD was humanized), and *mo*PD-1^{PEQ} (whose pre-ITSM sequence [H] was replaced with the human version [PEQ]), together with the cell surface marker Thy1.1, during in vitro anti-*mo*CD3ε/anti-*mo*CD28 stimulation. The three versions of exoPD-1 were expressed at comparable levels, as evidenced by flow cytometry (Fig. 5B). We then adoptively transferred the primed, gene-modified P14 CD8$^+$ T cells into mice inoculated with B16.gp33 melanoma cells, which presented gp$_{33-41}$ peptide via H-2D^b. Tumors grew fastest in mice transferred with *mo*PD-1^{huICD}–expressing P14 cells (P14–*mo*PD-1^{huICD}) and slowest in mice transferred with *mo*PD-1^{WT}–expressing P14 cells (P14–*mo*PD-1^{WT}). Intermediate tumor growth was seen in mice transferred with *mo*PD-1^{PEQ}–expressing P14 cells (P14–*mo*PD-1^{PEQ}) and in control mice that had not received P14 transfer (Fig. 5C). These results provide in vivo evidence that ICD humanization of *mo*PD-1 increases its T cell suppressive capacity, at least partly because of the pre-ITSM PEQ motif. The mechanism by which *mo*PD-1^{huICD}–expressing P14 cells accelerated tumor growth compared with the no-transfer control is unclear but suggests that *hu*PD-1 not only inhibits the antitumor activity of T cells, but also promotes tumor growth through other mechanisms. We confirmed these results using *Cas9*$^{+/-}$ P14 T cells, in which we deleted the endogenous PD-1 and reexpressed exogenous *mo*PD-1^{WT}, *mo*PD-1^{huICD}, and *mo*PD-1^{PEQ} using a retrovirus plasmid encoding a *Pdcd1*-targeting sgRNA, the exoPD-1 variant, and Thy1.1 (fig. S9). These data validated the stronger inhibitory activity of *hu*PD-1^{ICD} and the significance of the pre-ITSM PEQ motif.

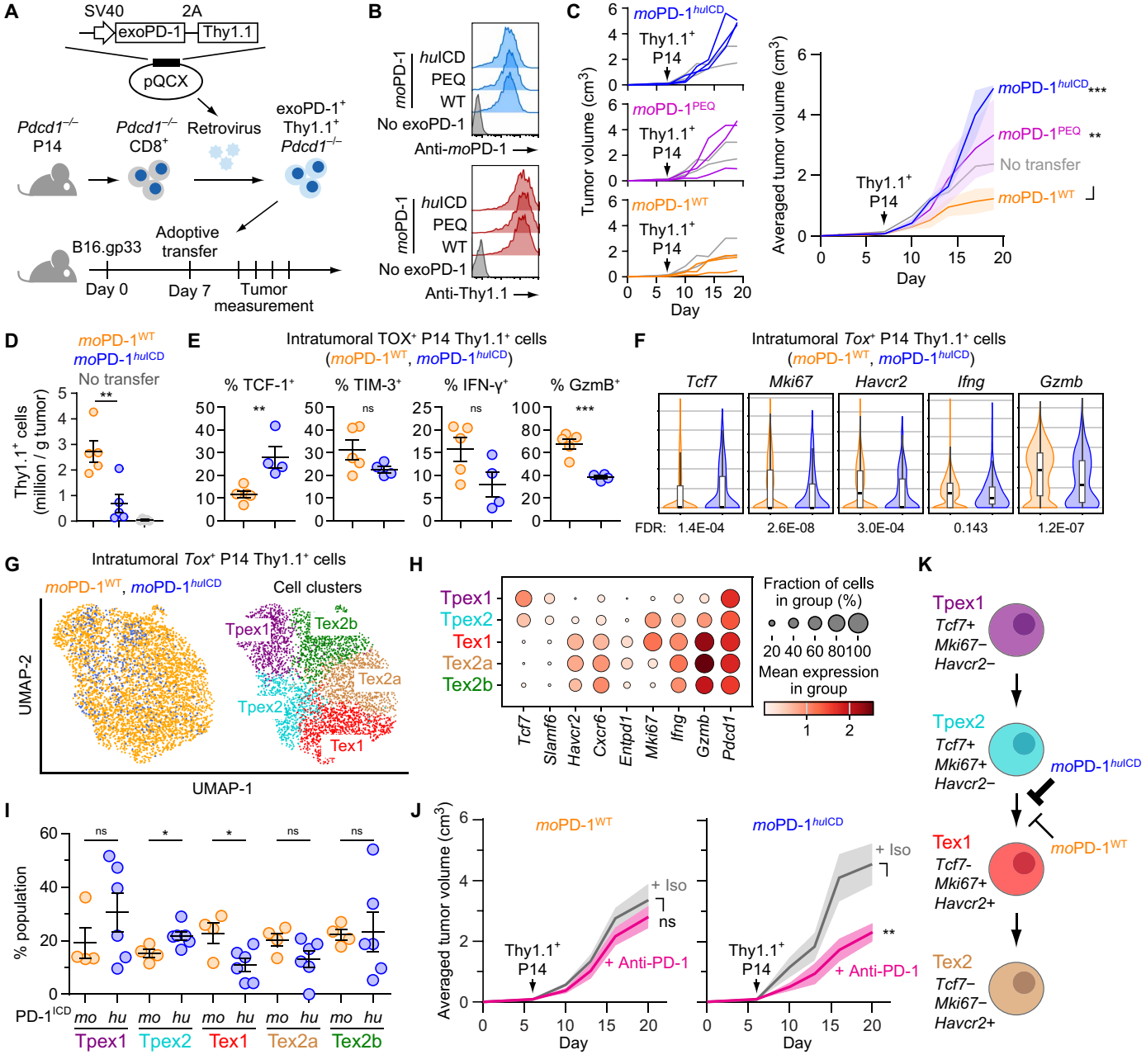

Fig. 5. ICD humanization of *mo*PD-1 inhibits precursor-to-terminal differentiation of *Tox*$^+$ CD8$^+$ T cells. (**A**) Schematic of an adoptive transfer experiment using *Pdcd1*$^{-/-}$ P14 CD8$^+$ T cells and B16.gp33 cells. *Pdcd1*$^{-/-}$ P14 cells were retrovirally transduced with exoPD-1 and Thy1.1 and adoptively transferred to mice bearing B16.gp33 melanoma. (**B**) Surface staining of indicated *mo*PD-1 variants and Thy1.1 on P14 cells transferred to mice in (A). (**C**) Tumor growth curves in mice received 1 million *Pdcd1*$^{-/-}$ P14 cells expressing either *mo*PD-1^{WT} or *mo*PD-1^{huICD} ($n = 2$ or 3 mice). (**D**) Number of Thy1.1$^+$ intratumoral CD8$^+$ T cells ($n = 5$ tumors). (**E**) % TCF-1$^+$, % TIM-3$^+$, % IFN-γ$^+$, and % GzmB$^+$ population within TOX$^+$ intratumoral P14 cells containing either *mo*PD-1^{WT} or *mo*PD-1^{huICD}, based on flow cytometry ($n = 4$ or 5 tumors). (**F**) Expressions of the indicated genes in *Tox*$^+$ intratumoral P14 cells containing either *mo*PD-1^{WT} or *mo*PD-1^{huICD}, based on scRNA-seq. (**G**) UMAP showing the *Tox*$^+$ intratumoral P14 cells containing either *mo*PD-1^{WT} or *mo*PD-1^{huICD} and their cell clusters. (**H**) Dot plot of indicated gene expressions in the cell subsets identified in (G). (**I**) Percent population of the indicated subsets of intratumoral P14 cells containing either *mo*PD-1^{WT} or *mo*PD-1^{huICD} ($n = 4$ to 6 tumors). (**J**) B16.gp33 tumor growth curves in mice that received 1.2 million P14 cells containing *mo*PD-1^{WT} (left) or *mo*PD-1^{huICD} (right), in response to treatment of either anti–PD-1 (blue) or isotype control (magenta) ($n = 7$ mice per group). (**K**) Model showing how PD-1 humanization affects the precursor-to-terminal differentiation of *Tox*$^+$ intratumoral CD8$^+$ T cells. Data are mean ± SEM calculated on the basis of the numbers of mice or tumors indicated above [(C), (D), (E), (I), and (J)]. For violin box plots (F), black bars are median, the boxes are 25% to 75% interquartile range, and the whiskers stand for minimum to maximum values excluding outliers. *$P < 0.5$; **$P < 0.01$; ***$P < 0.001$; ns, not significant; two-way ANOVA [(C) and (J)], Student's *t* test [(D), (E), and (I)], or Wilcoxon signed-rank test [(F)]. FDR was calculated using the Scanpy toolkit.

PD-1–ICD humanization accumulates the stem-like precursor exhausted T cells and lead to a stronger anti–PD-1 response

To further investigate the cellular mechanism underlying the altered antitumor response associated with PD-1 humanization, we characterized intratumoral T cells via flow cytometry and single-cell RNA sequencing (scRNA-seq). Flow cytometry showed that PD-1–ICD humanization decreased the number of intratumoral P14 T cells (Fig. 5D and fig. S10) and their expression of granzyme B (GzmB), but did not alter their expression of interferon-γ (IFN-γ) or the exhaustion marker TOX (fig. S11A). Consistent with the flow cytometry results, scRNA-seq detected eightfold more intratumoral P14 cells in mice receiving P14 (*mo*PD-1^{WT}) than in mice receiving P14 (*mo*PD-1^{huICD}) (fig. S11, B and C). Gene expression analysis revealed that PD-1–ICD humanization significantly reduced the expression of *Gzmb* and *Mki67*, but not *Tox*, in intratumoral P14 T cells (fig. S11D). Uniform manifold approximation and projection (UMAP) identified five cell clusters, Tox^+ clusters 0 to 2 and Tox^- clusters 3 and 4 (fig. S11E). PD-1–ICD humanization did not alter the proportion of total Tox^+ cell population (clusters 0 to 2), but increased the Tox^+Tcf7^+ subset (cluster 2) at the expense of Tox^+Tcf7^- subsets (clusters 0 and 1) (fig. S11F). These data indicate that PD-1–ICD humanization alters the differentiation within the Tox^+ T cell population, a notion further supported by flow cytometry analysis at the protein level (Fig. 5E). Further scRNA-seq analysis of the Tox^+ population revealed that PD-1–ICD humanization decreased *Mki67*, *Havcr2*, and *Gzmb* but increased *Tcf7* expression (Fig. 5F). UMAP of Tox^+ cells identified five subsets (Fig. 5, G and H): Subset 1 expressed *Tcf7* and *Slamf6*, but lacked *Mki67*, consistent with a precursor-exhausted-1 T cell (Tpex1) signature; subset 2 expressed *Tcf7*, *Slamf6*, and *Mki67*, consistent with a Tpex2 signature. Subsets 3 to 5 lost *Tcf7* but acquired *Havcr2* (TIM-3), *Cxcr6*, and *Entpd1* (CD39) expression. Subset 3 maintained *Mki67* expression, consistent with a terminally exhausted-1 T cell (Tex1) signature. Subsets 4 and 5 were devoid of *Mki67*, consistent with a Tex2 signature (*43*), but differed in their cell cycle phases (fig. S12), and were thus designated as Tex2a and Tex2b (Fig. 5, G and H). PD-1–ICD humanization reduced the Tex1 population, known to exhibit effector functions (*43*), while increasing the precursor-exhausted populations with less effector function (Fig. 5I). These data indicate that PD-1–ICD humanization inhibited the Tpex2-to-Tex1 differentiation, potentially contributing to the lack of tumor control (Fig. 5C and fig. S9D). Anti–PD-1 treatment elicited significant tumor control in mice receiving P14–*mo*PD-1^{huICD}, but not in mice receiving P14–*mo*PD-1^{WT} (Fig. 5J and fig. S13), consistent with the relative abundance of Tpex in these two settings and prior reports that Tpex is the primary mediator of anti–PD-(L)1 response (*44*–*47*). Altogether, our data suggest that *hu*PD-1 more potently restricts the proliferation, effector function, and precursor-to-terminal transition of exhausted T cells compared with *mo*PD-1 (Fig. 5K).

Rodent PD-1 orthologs share a weak pre-ITSM motif

The functional relevance of the PEQ motif in *hu*PD-1 motivated us to explore its divergence among vertebrates. We created a phylogenetic tree on the basis of the amino acid sequence alignment of full-length PD-1 from 236 vertebrates, including amphibians, reptiles, birds, and mammals, color-coded on the basis of on the pre-ITSM sequence (Fig. 6A; see Materials and Methods). The PEQ motif found in *hu*PD-1 is conserved in 131 species. In an additional 71 species, PD-1 orthologs contain PEQ-like motifs in the same region (Fig. 6A). In contrast, PD-1 orthologs in the entire rodent clade contain a lone His at the pre-ITSM position (Fig. 6A).

We next examined the biochemical consequences of different pre-ITSM sequences in a cell-SLB setup (Fig. 4A). We transduced Jurkat cells with *hu*PD-1 mutants in which the PEQ motif was replaced with the pre-ITSM motif found in other PD-1 orthologs and measured Shp2 recruitment to PD-1 microclusters in anti-*hu*CD3ε/*hu*ICAM1/*hu*PD-L1 stimulated Jurkat cells (Fig. 6B). TIRF-M showed that *hu*PD-1 with rodent pre-ITSM sequence (His) recruited significantly less Shp2 than did *hu*PD-1 with PEQ or PEQ-like pre-ITSM sequences.

We further evaluated the correlation between pre-ITSM sequences and PD-1 signaling strength across five mammalian species: three nonrodent species (human, monkey, and dog) containing the PEQ motif and two rodents (mouse and rat) with a His (fig. S14A). To compare the intracellular signaling of these PD-1 orthologs, we created four PD-1 chimeras by replacing the ICD of *hu*PD-1 with the ICD of monkey, dog, mouse, or rat PD-1. We then engineered five Jurkat cell lines expressing either *hu*PD-1 or each of the four chimeras at similar levels. Notably, these PD-1 variants were identical in their ECD and TMD (human) and, therefore, could be triggered by *hu*PD-L1–expressing Raji cells and blocked by atezolizumab. Human IL-2 enzyme-linked immunosorbent assay (ELISA) showed that *hu*PD-1 and chimeras with PEQ-containing ICDs (derived from monkey and dog PD-1) inhibited IL-2 production by ~60%, whereas chimeras with mouse or rat ICDs were significantly less inhibitory (35 to 40%) (fig. S14B). Collectively, our data suggest that the pre-ITSM sequence predicts the signaling strength of PD-1 orthologs and that rodent PD-1 orthologs have weaker activity because of the lack of a PEQ-like motif.

Functional attenuation of PD-1 during rodent evolution

The weaker PD-1 function in rodents suggested that taxon-specific events and selection effects occurred during rodent evolution. To explore this further, we aligned PD-1 sequences from 107 mammalian species, including 19 rodents from all four major suborders (2 from Hystricomorpha, 1 from Sciuromorpha, 3 from Castorimorpha, and 13 from Myomorpha). On the basis of the tree topology of mammal phylogeny, we conducted maximum likelihood inference of positive selection and relaxation on different combinations of tree branches in both the rodent and primate lineages (see Materials and Methods). At the basal branch [most recent common ancestor (MRCA)] of all rodents, we found significant positive selection ($P < 0.02$ by BUSTED program) (*48*). The same is true for MRCA of primates ($P < 0.003$). All branches within the rodent clade exhibited significant relaxation of selection pressure ($k = 0.8$, $P < 0.05$ by RELAX program) (*49*), which was not found in primates ($k = 1.0$, $P > 0.5$) (table S1). These results indicate a lineage-specific relaxation of selection pressure on PD-1 during rodent evolution, suggesting gradual attenuation of PD-1 function within the rodent clade. Conversely, other inhibitory immunoreceptors such as BTLA, TIGIT, LAG3, and PVRIG showed that either positive selection or selection intensification was observed within the rodent clade (table S1).

To validate this potential trajectory of functional change, we next performed ancestral sequence reconstruction (ASR) of PD-1 for seven key evolutionary time points in the tree (nodes with numerical IDs in Fig. 6C; predicated amino acid sequences are shown in table S2), following common practices of ASR (*50, 51*) (see Materials and Methods). For each node, we replaced the ICD sequence of *hu*PD-1 with the reconstructed ancestral PD-1 ICD, expressed the chimera

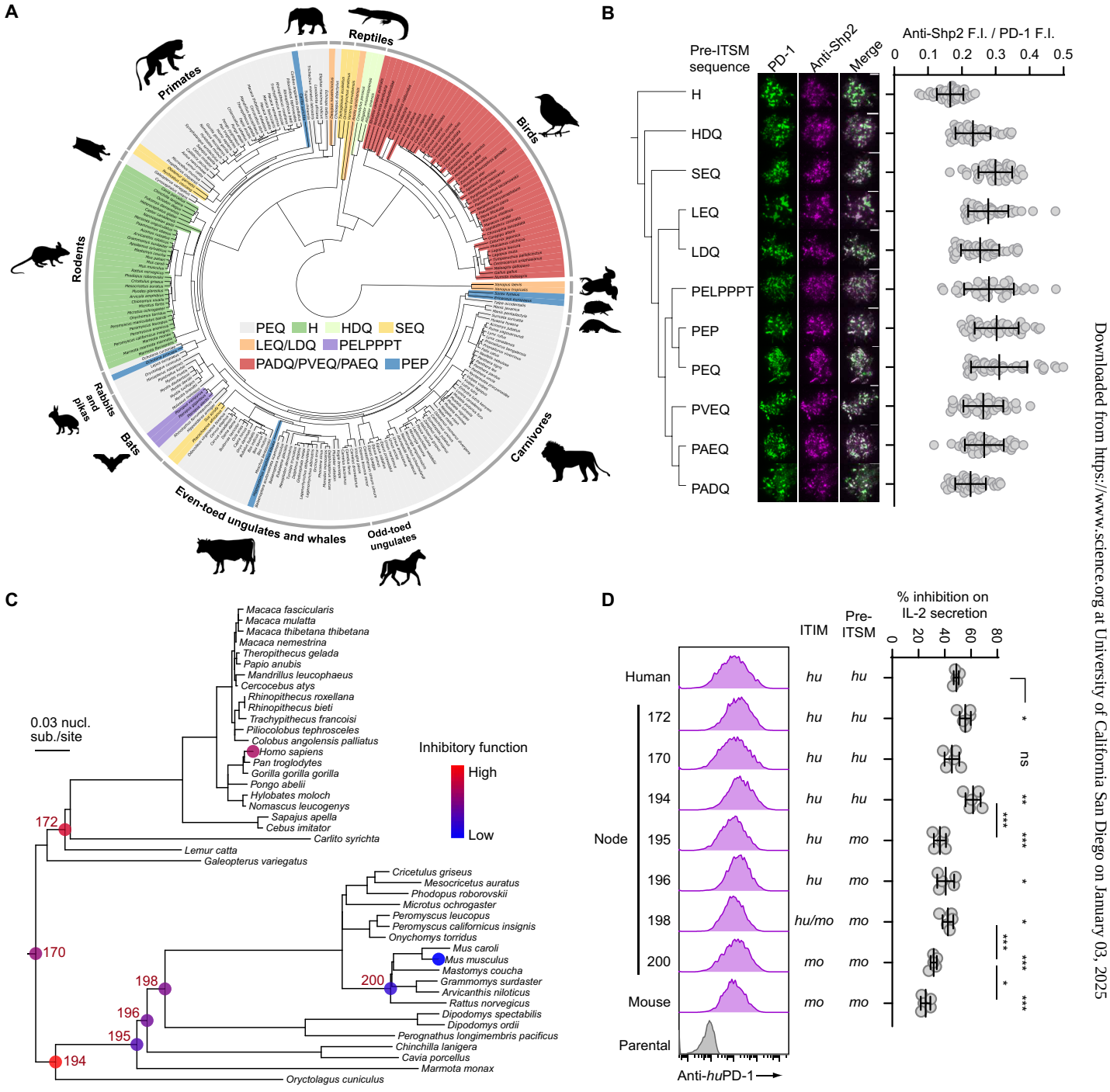

Fig. 6. Rodent PD-1 orthologs share a distinct pre-ITSM sequence that weakens their ability to recruit Shp2. (**A**) Phylogeny of 236 vertebrate species, color-coded on the basis of the pre-ITSM sequence of PD-1. (**B**) Left: A phylogenetic tree of pre-ITSM sequence found in PD-1 orthologs. Middle: Representative TIRF images of microclusters of the GFP-tagged *hu*PD-1 variant bearing the indicated pre-ITSM sequence (green) and endogenous Shp2 (magenta) in an anti-*hu*CD3ε/*hu*PD-L1 stimulated Jurkat cell. Right: Dot plots showing anti-Shp2 F.I. normalized to PD-1 F.I. in Jurkat cells expressing the indicated *hu*PD-1 variant ($n = 40$ cells). Scale bars, 5 μm. (**C**) The subtree of the 107-species mammal phylogeny spanning the rodent clade and the primate clade. The branch lengths were inferred on the basis of PD-1 codon sequence evolution. The marked nodes are mouse, human, or the ones with reconstructed ancestral sequences. The color codes show the inhibition ability of the sequences at respective nodes, based on data in (D). The bar indicates 0.03 nucleotide substitutions per codon site. (**D**) Left: FACS histograms showing the expression of *hu*PD-1 chimera harboring an ICD corresponding to the indicated node, on Jurkat cells. Right: % inhibition of IL-2 secretion by the indicated *hu*PD-1 chimera upon stimulating Jurkat (*hu*PD-1 chimera) with Raji cells (*hu*PD-L1). The ITIM type and pre-ITSM type are labeled: *hu*, humanlike; *mo*, mouselike ($n = 5$ independent technical replicates). Data are mean ± SD calculated on the basis of the sample numbers indicated in each panel. *$P < 0.05$; **$P < 0.01$; ***$P < 0.001$; ns, not significant; Student's *t* test.

in Jurkat cells, and examined its ability to suppress IL-2 secretion upon coculture with SEE-pulsed *hu*PD-L1–expressing Raji cells. We found that whereas the inhibitory capacities of the primate MRCA (node 172) and the shared MRCA of rodents and primates (node 170) were comparable to that of *hu*PD-1, the inhibitory capacities of PD-1 decreased along the evolution trajectory within the rodent lineage, from the MRCA of rodent and rabbit (node 194) to modern mice (Fig. 6D). Specifically, the transition of pre-ITSM PEQ to H at the MRCA branch of all rodents (node 195, 60 to 65 million years ago in Paleogene, right after the K-Pg boundary extinction event ~66 million years ago) (*52*, *53*) introduced a major decrease in PD-1 inhibitory capacity. This was followed by additional attenuation between nodes 198 and 200 and between node 200 and modern mice. These sequential events indicate a gradual attenuation of PD-1 function within the rodent lineage, suggesting a rodent-specific change of selection pressure during evolution.

DISCUSSION

Using quantitative assays, we document herein that *mo*PD-1 has a weaker activity than all other PD-1 orthologs tested. Specifically, we found that the weaker activity of *mo*PD-1 compared with *hu*PD-1 mapped to both the ECD and ICD. Despite only 58% amino acid identity in their ICDs, *hu*PD-1 and *mo*PD-1 are often assumed to have conserved activity because of their identical ITSM, the main Shp2 docking site. However, we show that *mo*PD-1 ICD is intrinsically less inhibitory than *hu*PD-1 ICD, and humanizing the PD-1 ICD impaired $CD8^+$ T cell antitumor activity. Thus, *hu*PD-1 could potentially serve as a gain-of-function mutant for future PD-1 research in mouse models, although qualitative functional differences in *hu*PD-1 versus *mo*PD-1 cannot be ruled out.

Mechanistically, the lack of tumor control by P14 cells expressing ICD-humanized PD-1 involved multiple factors, including the markedly decreased intratumoral T cell numbers, lower effector function, and the altered T cell subset landscape (e.g., increased Tpex-to-Tex ratio). This notion aligns with the stronger anti–PD-1 response in mice containing ICD-humanized PD-1. These functional differences might contribute to the observed differential response to PD-(L)1 inhibitors in mouse models and human patients, among other mechanisms.

Considering the role of PD-1 in peripheral tolerance and autoimmunity prevention (*1*, *4*, *16*, *18*, *54*), our findings indicate that loss of PD-1 activity may provoke stronger autoimmune phenotypes in humans than in mice. Inherited PD-1 deficiency in humans led to early death from pneumonitis in two siblings (*18*). Moreover, anti–PD-1 treatment in humans results in grade > 3 adverse reactions in 10% and any-grade toxicity in 20% of patients (*55*, *56*). In contrast, mouse models of anti–PD-1 do not show adverse events seen in patients unless bred onto an autoimmune susceptibility locus (*57*). In addition, PD-1 deficiency in the C57BL/6 strain causes lupus-like autoimmunity only in aged mice (>1 year) or when combined with the *lpr* mutation that promotes lymphoproliferation (*58*). Notably, however, PD-1 deficiency in the BALB/C strain causes dilated cardiomyopathy and early death by 5 weeks of age (*59*), indicating that strain background could influence PD-1 function in laboratory mice. Whereas human versus mouse differences in PD-1 deficiency penetrance and phenotype could stem from the strain, inbred nature, and specific pathogen–free housing conditions of laboratory mice, our studies suggest that the gene itself may also contribute to this variation.

Humanized PD-1 mouse models are valuable for preclinical testing of human checkpoint inhibitors, but often express a chimeric PD-1 with only the ECD humanized, leaving the ICD murine. Although these models can respond to human PD-1 inhibitors, the intrinsic differences in the intracellular signaling of *hu*PD-1 versus *mo*PD-1 highlighted in this study suggest that full-length *hu*PD-1 knockin mice would be more suitable for modeling human PD-1 signaling and responses to anti–*hu*PD-1 therapy.

The poorly conserved PD-1 sequence in humans and mice contrasts with the highly conserved Shp2 sequence, but this appears to reflect a common feature of many signaling pathways, with receptors being less conserved and intracellular effectors more conserved. Other examples include the following: CD28 and its effector PKCθ (*60*), which exhibit 68.8 and 95.0% sequence identities, and BTLA and its effector Shp1 (*61*), which exhibit 49.2 and 94.5% sequence identities between human and mouse orthologs. Because intracellular effectors are often shared by multiple signaling pathways (*62*), their high conservation might be essential for maintaining cellular signaling network stability during evolution. Meanwhile, evolving receptor sequences would offer a more specific and cost-effective means to modify the functional outcomes of a particular signaling axis.

Whereas conserved sequences often predict biological importance, our study highlights that sequence variations can also inform biological insights. Guided by this concept, we identify two motifs (PEQ and PRS), along with ITIM, that modulate PD-1 biochemistry and function. The PEQ motif, which is immediately upstream of ITSM in *hu*PD-1 and altered to a single His in *mo*PD-1, is primarily responsible for the stronger Shp2 binding activity of *hu*PD-1. The recently reported *hu*PD-1–ITSM:Shp2 structure revealed hydrogen bonds between pre-ITSM residues and the SH2 domains of Shp2 (*63*). The N-terminal phosphotyrosine motif ITIM, known as the secondary Shp2 docking site, also appeared to be weakened in rodent PD-1. These results might explain some of the discrepancies regarding the reported roles of ITIM in PD-1 function. The PRS motif, with two extra prolines in *hu*PD-1, might regulate Shp2 binding through orienting ITIM and ITSM. The divergence of these motifs confers functional plasticity in PD-1 orthologs and offers avenues to engineer PD-1 variants with desired functional properties.

The importance of the PEQ motif in PD-1 is underscored by its perfect conservation in 131 of 146 nonrodent mammalian species analyzed, with the remaining 11 nonrodent mammals and all other 56 vertebrate species containing PEQ-like motifs in the corresponding region. Rodent PD-1 orthologs are exceptions, with this motif replaced by a single His, which our data suggest is the primary reason for their weaker inhibitory activities compared with PD-1 in other mammals. We further show that PD-1 continued to undergo relaxation and weakening throughout rodent evolution, though the reason for the rodent-specific PD-1 devaluation is unclear. Given that a weaker PD-1 pathway might increase the strength and duration of immune responses and that this seemed to have occurred at the time of a major extinction event, it is possible that weakening PD-1 afforded rodents with the ability to adapt to special ecological niches and selective pressures from rodent-specific pathogens.

In vivo experiments in this study relied on adoptively transferred T cells that recognize a model antigen. Future studies will assess the impact of PD-1 humanization on antitumor responses of endogenous T cells and its effects across various tumor types.

MATERIALS AND METHODS

Study design

The objective of this study was to conduct a cross-species comparison of the inhibitory immunoreceptor PD-1, which is only moderately conserved between humans and mice. To achieve this, we established a T cell: APC coculture assay to compare the inhibitory activities of human and mouse PD-1. We then used a combination of domain swapping, site-directed mutagenesis, protein binding assays, and cellular imaging to examine the molecular mechanisms underlying the differential inhibitory activities of human and mouse PD-1. Next, to assess the impact of PD-1 humanization on $CD8^+$ T cell antitumor immunity, we used a mouse melanoma model with adoptively transferred $CD8^+$ T cells expressing either wild-type or ICD-humanized mouse PD-1. We measured the tumor growth as well as analyzed the abundance, effector functions, and differentiation of intratumoral T cells using flow cytometry and scRNA-seq. Last, we conducted evolutionary analysis, particularly ASR, to compare the evolutionary trajectories of PD-1 across the rodent and primate lineages. Details on randomization and blinding of the in vivo experiments are described in the "Adoptive transfer experiments" section. The number (n) of biological or technical replicates is indicated in the figure legends.

Reagents

cDNA of rat PD-1 (#RG80448-G), dog PD-1 (#DG70109-G), and monkey PD-1 (#KG90305-G) was purchased from Sino Biological. $OVA_{323\text{-}339}$ peptide (#AS-27024) was purchased from Anaspec. Recombinant human IL-2 (#200-02) and recombinant mouse IFN-γ (#315-05) were purchased from PeproTech. Staphylococcal enterotoxin E (SEE, #ET404) and staphylococcal enterotoxin B (SEB, #BT202) were purchased from Toxin Technology. RPMI 1640 medium (#10-041-CM) was purchased from Corning. Dulbecco's minimum essential medium (#MT10017CV), MEM nonessential amino acids solution (NEAA: #11140050), sodium pyruvate (#11360070), Alexa Fluor 647 NHS ester (AF647 NHS ester: #A37573), Ni-NTA agarose (#88223), Zeba Spin Desalting Columns (#89890), dynabeads T-activator CD3/CD28 (#11132D), polyethyleneimine (PEI: #NC1014330), and saponin (#558255) were purchased from Thermo Fisher Scientific. Fetal bovine serum (FBS: #FB-02) was purchased from Omega Scientific. Penicillin-streptomycin (P/S) (1×; #SV30010) and Ficoll-Paque (#17544202) were purchased from Cytiva. SHP099 (#S8278) was purchased from Selleck Chemicals. FuGENE transfection reagent (#E2691) was purchased from Promega. Polybrene transfection reagent (#TR-1003-G) was purchased from EMD Millipore. Brefeldin A (#00-4506-51) and the transcription factor staining kit (#00-5523-00) were purchased from eBioscience. Ghost Dye Red 780 (#18452) was purchased from Cell Signaling Technology. Hellmanex (#Z805939) was purchased from Sigma-Aldrich. Paraformaldehyde (PFA; #15714) was purchased from Electron Microscopy Sciences. Glutathione agarose 4B (#G-250-50) was purchased from Gold Biotechnology. The MojoSort human CD4 T cell isolation kit (#480009), the MojoSort human CD8 T cell isolation kit (#480012), the MojoSort mouse CD8 T cell isolation kit (#480007), the human IL-2 ELISA kit (#88702577), and the mouse IL-2 ELISA kit (#431001) were purchased from BioLegend. SnapCell505 star (SC505: #S9103S) was purchased from NEB. DiD (#60014) was purchased from Biotium. Superdex 75 Increase column (#GE29-1487-21) and Superdex 200 Increase column (#GE28-9909-44) were purchased from GE Healthcare. The Quantum PE MESF kit (#827) was purchased from Bangs Laboratories. Glass-bottom 96-well plate (#P96-1.5H-N) was purchased from Cellvis. Collagenase (#LS004197) and soybean trypsin inhibitor (#LS003587) were purchased from Worthington Biochemical. eBioscience Foxp3/Transcription Factor Staining Buffer Set (#00-5523-00) was purchased from Invitrogen. Chromium Next GEM Single Cell 3′ Reagent Kit v3.1 (Dual Index) with Feature Barcode Technology for Cell Surface Protein was purchased from 10x Genomics.

Antibodies

Biotin anti-human CD3ε (clone OKT3, #317320) and biotin anti-mouse CD3ε (clone 145-2C11, #100303), APC anti-human CD69 (clone FN50, #310910), Alexa Fluor 700 anti-mouse CD8a (clone53-6.7, #100729), BV711 anti-mouse IFN-γ (clone XMG.12, #505835), FITC anti-mouse CD8 (clone 16-10A1, #104705), BV785 anti-mouse CD8 (clone 53-6.7, #100750), PerCP/Cyanine5.5 anti-mouse CD8 (clone 53-6.7, #100734), PerCP/Cyanine5.5 anti-mouse CD45 (clone 30-F11, #103132), FITC anti-mouse Thy1.1 (clone OX-7, #202503), BV785 anti-mouse Tim3 (clone RMT3-23, #119725), FITC anti-mouse TCR Vα2 (clone B20.1, #127805), Alexa Fluor 647 anti-mouse Thy1.1 (clone OX-7, #202507), PE/Cyanine7 anti-human CD3 (clone UCHT1, #300419), APC anti-human CD4 (clone RPA-T4, #300552), PE anti-mouse CD8 (clone 16-10A1, #104707), and customized TotalSeq-anti-mouse Hashtag Antibodies devoid of anti-CD45 (#155831, #155833, #155835, #155839, #155841, and #155843) were purchased from BioLegend. Anti-Shp2 (clone 79, #BDB610621) and BV605 anti-mouse Ly108 (clone 13G3, #745250) were purchased from BD Biosciences. Anti-mouse CD3ε (clone 145-2C11, #BE0001-1), anti-mouse CD28 (clone 37.51, #BE0015-1), InVivoMAb anti-mouse PD-1 (clone J43, #BE0033-2), and InVivoMAb polyclonal Armenian hamster immunoglobulin G (IgG) (polyclonal, #BE0091) were purchased from Bioxcell. PE anti-human PD-1 (clone MIH4, #12-9969-42) and PE-anti TOX (clone TXRX10, #12-6502-82) were purchased from Invitrogen. Pembrolizumab (#A2005) and atezolizumab (anti–PD-L1, #A2004) were purchased from Selleck Chemicals. PE-Cy7 anti-mouse PD-1 (clone J43, #25-9985-82) and PE anti-mouse Thy1.1 (clone HIS51, #12-0900-83) were purchased from eBioscience. Alexa Fluor 647 anti-TCF1/TCF7 (clone C63D9, #6709S) was purchased from Cell Signaling Technology. Goat IgG fraction-anti-mouse IgG (#08670281) was purchased from MPbio. For TIRF imaging of Shp2 in Figs. 4 and 6, anti-Shp2 was labeled using AF647 NHS ester. The unreacted dye was removed via buffer exchange using a Zeba Spin Desalting Column (Thermo Fisher Scientific) and eluted with Hepes buffer saline (50 mM Hepes-NaOH, pH 7.5, 150 mM NaCl, and 10% glycerol), following the manufacturer's instructions. The purified antibody was stored at −80°C until use.

Lipids

1-Palmitoyl-2-oleoyl-glycero-3-phosphocholine (POPC; #850457), 1,2-dioleoyl-sn-glycero-3-[(*N*-(5-amino-1-carboxypentyl) iminodiacetic acid)succinyl] (nickel salt) (DGS-NTA-Ni; #790404), 1,2-dipalmitoyl-sn-glycero-3-phosphoethanolamine-*N*-(lissamine rhodamine B sulfonyl) (ammonium salt) (Rhodamine-PE; #810158), 1,2-dipalmitoyl-sn-glycero-3-phosphoethanolamine-*N*-(biotinyl) (sodium salt) (Biotinyl-PE; #870285), and 1,2-dioleoyl-sn-glycero-3-phosphoethanolamine-*N*-[methoxy(polyethylene glycol)–5000] (ammonium salt) (PEG5k-PE; #880230) were purchased from Avanti Polar Lipids. *N*-(4,4-Difluoro-5,7-dimethyl-4-bora-3a,4a-diaza-s-indacene-3-propionyl)-1,2-dihexadecanoyl-sn-glycero-3-

phosphoethanolamine (triethylammonium salt) (Bodipy-PE; #D3800) was purchased from Thermo Fisher Scientific.

Chimeric protein design

To construct *hu*PD-1–based chimeras, *hu*PD-1 ECD (amino acids 24 to 170), TMD (amino acids 171 to 191), or ICD (amino acids 192 to 288) was replaced with the corresponding domain of *mo*PD-1 (ECD: amino acids 25 to 169, TMD: amino acids 170 to 193, ICD: amino acids 194 to 288), rat PD-1 (ICD: amino acids 194 to 287), dog PD-1 (ICD: amino acids 195 to 288), monkey PD-1 (ICD: amino acids 192 to 288), or reconstructed ancestral PD-1 (table S2). *mo*PD-1–based chimeras were designed in the same fashion using *mo*PD-1 as a template. To construct GFP^{ECD}–$PD\text{-}1^{ICD}$ chimeras, an N-terminal signal peptide of beta 2 microglobulin (MSRSVALAVLALLSLSGLEA), mGFP, human CD86 stalk-TMD region (amino acids 236 to 271), and *hu*PD-1 ICD or *mo*PD-1 ICD were fused in sequence. To construct GFPNb-TMD-TagBFP, GFPNb, an N-terminal signal peptide of beta 2 microglobulin (MSRSVALAVLALLSLSGLEA), the Fc region of human IgG1 (amino acids 100 to 228), human CD86 stalk-TMD region, and TagBFP were fused in sequence.

Mice

Cas9 mice were procured from the Jackson Laboratory (B6(C)-Gt(ROSA)26Sorem1.1(CAG-cas9*,-EGFP)Rsky/J) and crossed with $P14^+$ transgenic mice to generate $Cas9^{+/-}$ P14 mice. $Pdcd1^{-/-}$ P14 mice were provided by R. Ahmed (Emory University). B6 mice were bred in house. All animals were housed under specific pathogen–free conditions at the University of California San Diego (UCSD). All procedures were previously reviewed and approved by the UCSD Institutional Animal Care and Use Committee under protocol S06201.

Cell lines and cultures

Jurkat E6-1 cells (#TIB-152) and A20 cells (#TIB-208) were purchased from the American Type Culture Collection (ATCC). HEK293T cells and Raji B cells were provided by R. Vale (University of California San Francisco). Phoenix cells were provided by F. Kai (University of California San Francisco). DO11.10 T cell hybridoma was provided by P. Marrack (National Jewish Health Center). HEK293T, Phoenix, and B16.gp33 cells were maintained in Dulbecco's modified Eagle's medium supplemented with 10% FBS and 1× P/S. Human-derived Jurkat cells and Raji B cells were maintained in RPMI medium supplemented with 10% FBS and 1× P/S. Mouse-derived DO11.10 T cell hybridoma and A20 cells were maintained in RPMI medium supplemented with 10% FBS, 1× P/S, and 50 μM β-mercaptoethanol. All cells were cultured in a 37°C/5% CO_2 incubator.

Cell line gene transduction and knock out

The gene of interest (GOI) was transduced into Jurkat cells and Raji B cells via lentivirus transduction or into DO11.10 T cell hybridoma and A20 cells via retrovirus transduction. Lentivirus and retrovirus were prepared as previously described (*34*). For lentivirus production, GOI was cloned into pHR vector and cotransfected into HEK293T cells with envelope/packaging plasmids (pMD2.G and psPAX2) using PEI. For retrovirus production, GOI was cloned into pMIG II vector and transfected into Phoenix cells together with the pCL-Eco packaging plasmid using PEI. The virus supernatants were harvested 60 to 72 hours after transfection, centrifuged to remove the contaminated cells, and mixed with target cells for transduction. To ensure similar expression of PD-1 variants for quantitative comparisons, intrinsically high-expressing constructs were transduced with diluted virus supernatant to reduce the expression level, whereas intrinsically low-expressing constructs were reinfected to increase the expression level. The virus-containing media were replaced with fresh RPMI media 3 to 5 days after transduction. The cells expressing GOI were sorted using a FACS Aria flow cytometer (BD). Gene knockout was performed using the CRISPR-Cas9 technique. Target cell lines were electroporated with pX330 vector using Gene Pulser Xcell (Bio-Rad). After the electroporation, the cells were cultured for 2 to 3 days and stained with corresponding antibodies to sort knocked-out cells using a FACS Aria flow cytometer (BD).

Purification, culture, and transduction of human primary T cells

Human primary T cells were obtained from blood samples of healthy donors (San Diego Blood Bank) via a density gradient method and magnetic bead purification. Briefly, human peripheral blood mononuclear cells (*hu*PBMCs) were isolated from blood samples of healthy donors and enriched by Ficoll-Paque gradient centrifugation. The $CD4^+$ or $CD8^+$ T cells in the purified *hu*PMBCs were isolated using the MojoSort Human CD4 T Cell Isolation Kit or MojoSort Human CD8 T Cell Isolation Kit (BioLegend) following the manufacturer's instructions. The >95% purity of the isolated T cells was confirmed via flow cytometric staining for the $CD3^+CD4^+$ or $CD3^+CD8^+$ population. The purified T cells were preactivated with Dynabeads T-Activator CD3/CD28 (Thermo Fisher Scientific) in the presence of human IL-2 (30 U/ml) for 2 days before gene transduction. The preactivated T cells were resuspended with lentivirus solution prepared as described above and subjected to spinofection at 1000*g* for 90 min at 32°C. Human primary T cells were maintained in RPMI medium supplemented with 10% FBS, 1× P/S, and human IL-2 (30 U/ml) in a 37°C/5% CO_2 incubator.

PD-1 CRISPR KO and reconstitution in mouse primary $Cas9^+$ $CD8^+$ T cells

For the in vivo experiments in fig. S9, splenocytes from $Cas9^{+/-}$ P14 female mice were obtained by mashing spleens and lymph nodes through a 70-μm cell strainer (BD). Naïve $CD8^+$ T cells were then enriched using the Mojosort mouse $CD8^+$ naïve T cell isolation kit (BioLegend). Purified naïve $CD8^+$ T cells were resuspended in RPMI medium supplemented with 5% FBS, 1 mM sodium pyruvate, 1× P/S, 1× nonessential amino acid solution, and 55 μM β-mercaptoethanol; activated using anti-mouse CD3ε (1 μg/ml) and anti-mouse CD28 (1 μg/ml); and incubated in a goat IgG fraction-anti-mouse IgG–coated plate at 37°C/5% CO_2 for 24 hours. Retrovirus pQCX plasmid encoding an exogenous *mo*PD-1 variant ($moPD\text{-}1^{WT}$, $moPD\text{-}1^{PEQ}$, or $moPD\text{-}1^{huICD}$), a P2A self-cleaving sequence, a Thy1.1 protein, and an sgRNA targeting endogenous *Pdcd1* were transfected to HEK293T cells using FuGENE transfection reagent following the manufacturer's instructions. Virus supernatants were harvested twice at 48 and 72 hours, respectively, sterilized through a 0.45-μm filter (Millipore Sigma), incubated with the stimulated $CD8^+$ T cells, and centrifuged at 1000*g* for 90 min at 32°C for spinfection. After removal of the virus-containing supernatant, cells were further cultured in the same RPMI supplemented with human IL-2 (100 U/ml). After 72 to 96 hours, $Thy1.1^+$ cells were sorted and cultured in the same RPMI medium supplemented with human IL-2 (100 U/ml) for at least 48 hours before the adoptive transfer. DNA sequences of the exogenous *mo*PD-1

variants were silently mutated at the sgRNA-targeting site (ACACACGGCGCAATGACAG to ATACCAGAAGGAACGATTC).

*Calculation of endo*PD-1 *KO scores for CD8$^+$ T cells*

A DNA fragment of *Pdcd1* including the sgRNA-targeting site was amplified via polymerase chain reactions (PCRs) using genomic DNA of *Cas9*$^{+/-}$ CD8$^+$ T cells as templates and using a primer pair (forward primer: TTCTGCATTTCAGAGGTCCCC, reverse primer: CCACCCACCCTACTTTGGC). The sequences of the amplicons were read via Sanger sequencing and subjected to the ICE program to calculate the percentage of *Pdcd1*$^{-/-}$ cells (KO scores) (*64*).

PD-1 reconstitution in mouse primary Pdcd1$^{-/-}$ CD8$^+$ T cells

For experiments in Fig. 5 and figs. S10 to S13, CD8$^+$ T cells were isolated from *Pdcd1*$^{-/-}$ P14 mice, stimulated for 24 hours, and reconstituted with exogenous PD-1 variant (*mo*PD-1^{WT}, *mo*PD-1^{PEQ}, or *mo*PD-1^{huICD}) as described in the previous section, except using a retrovirus lacking the endogenous *Pdcd1* targeting sgRNA. Specifically, the retrovirus was produced using a pQCX plasmid encoding an exogenous *mo*PD-1 variant (*mo*PD-1^{WT}, *mo*PD-1^{PEQ}, or *mo*PD-1^{huICD}), a P2A self-cleaving sequence, and Thy1.1, without the sgRNA cassette.

Adoptive transfer experiments

B6 mice were subcutaneously injected with 0.5 to 1 million B16.gp33 melanoma cells. Seven days after the B16.gp33 injection, P14 CD8$^+$ T cells that were in vitro expanded for 7 days were transferred into the retro-orbital venous sinous in the B16.gp33-bearing mice under anesthesia [100 μl of 1× phosphate-buffered saline (PBS) containing a mixture of pharmaceutical grade ketamine and xylazine]. For measuring tumor growth, each tumor-bearing mouse was transferred with 1 million (Fig. 5C), 1.2 million (Fig. 5J and fig. S13), or 0.5 million (fig. S9) PD-1–edited P14 CD8$^+$ T cells. For measuring the effect of PD-1 blockade on tumor growth, 100 μg of anti–PD-1 (clone J43) or isotype control was intraperitoneally injected on days 3, 7, and 10 after T cell transfer. For measuring the absolute number of intratumoral Thy1.1$^+$ CD8$^+$ T cells shown in Fig. 5D, 2 million P14 CD8$^+$ T cells were transferred to each tumor-bearing mouse and harvested from tumors 6 days after the transfer. For characterizing intratumoral Thy1.1$^+$ CD8$^+$ T cells, 1 million (Fig. 5E and fig. S11A) or 2 million (Fig. 5, F to I, and fig. S11, C to F) P14 CD8$^+$ T cells were transferred to each host mouse and harvested from tumors 7 days after the transfer. Tumor sizes were measured twice or thrice per week by an investigator blinded to the identity of the animals. Sample size was determined by using at least seven animals per cohort when possible on the basis of power calculations. Animals were randomized within each cage to receive one or the other type of T cells. If an animal had too much distress or the tumor was too large, this animal was sacked before flow cytometry experiments. Animals that died for any reason were excluded from the experiment. For characterization of intratumoral P14 Thy1.1$^+$ T cells, tumors were harvested from mice on the indicated days, minced with razors, and digested with collagenase type I (1 mg/ml) and soybean trypsin inhibitor (1 mg/ml) in 1× Hanks' balanced salt solution at 37°C for 1 hour, filtered through a 70-μm cell strainer (BD), and resuspended in 1× PBS to prepare single-cell suspensions. The tumor single-cell suspension samples were subjected to Percoll gradient centrifugation at 800*g* for 10 min, after which CD8$^+$ T cells were isolated using a CD8 bead selection kit (BioLegend).

Flow cytometry analysis

For measuring protein expression on cell lines by antibody staining, cells were stained with the indicated antibodies following the manufacturer's instructions, washed with 1× PBS and resuspended in FACS buffer (PBS with 2% FBS), and subjected to flow cytometry analysis on an LSRFortessa X-20 cell analyzer (BD). For measuring protein expression using mGFP or mCherry fluorescence, cells were directly resuspended in FACS buffer and subjected to flow cytometry. The absolute amount of PD-1 surface expression on human primary CD4$^+$ T cells or on Jurkat cells was quantified using a Quantum PE MESF kit (Bangs Laboratories) following the manufacturer's instruction. Briefly, cells were stained with PE anti-human PD-1 antibody and analyzed on an LSRFortessa X-20 cell analyzer together with the bead standards.

For characterizing intratumoral Thy1.1$^+$ CD8$^+$ T cells shown in Fig. 5E and fig. S11A, the isolated intratumoral CD8$^+$ T cells were stimulated with phorbol 12-myristate-13-acetate (50 ng/ml) and ionomycin (0.5 μg/ml) in the presence of brefeldin A (5 μg/ml) at 37°C/5% CO_2 for 4 hours. After the stimulation, TILs were stained with Zombie Aqua Fixable Viability Dye (BioLegend, #423101) on ice for 15 min, with TruStain FcX antibody (BioLegend, #101319) for 30 min, and subsequently with the antibodies for surface and intracellular protein markers using the eBioscience Foxp3/Transcription Factor Staining Buffer Set following the manufacturer's instruction. Stained samples were analyzed on an LSRFortessa X-20 cell analyzer. The intratumoral Thy1.1$^+$ CD8$^+$ T cells were identified using the gates shown in fig. S10.

scRNA-seq sample preparation

An intratumoral CD8$^+$ T cell sample isolated from the tumor of each mouse was stained with Zombie Aqua Fixable Viability Dye (BioLegend, #423101) in 1× PBS on ice for 15 min and subsequently with BV785 anti-moCD8, PE anti-Thy1.1, and FITC anti-TCRVα2 (P14 TCR) in 1× PBS containing 2% FBS on ice for 30 min. Live CD8$^+$, Thy1.1$^+$, and TCRVα2$^+$ cells in each sample were sorted on FACSAria into different tubes containing RPMI 1640 with 5% FBS. The sorted cell samples were distributed into two groups: cell samples isolated from mice that received *mo*PD-1^{WT}–expressing P14 cells and cell samples isolated from mice that received *mo*PD-1^{huICD}–expressing P14 cells. Each cell sample in the same group was hash-tagged with a distinct TotalSeq anti-mouse MHC-I antibody (BioLegend) on ice for 30 min and washed with 1× PBS containing 2% FBS. After the hash-tagging, the cell samples in the same group were pooled into one tube and diluted in 1× PBS containing 2% FBS to 1 million/ml. Approximately 20,000 and 2000 cells were recovered in *mo*PD-1^{WT} or *mo*PD-1^{huICD} groups, respectively, all of which were subjected to library preparation. Both the gene expression (GEX) library and the hash-tag library of each group were prepared using a Chromium Next GEM Single Cell 3′ Reagent Kits v3.1 (Dual Index) with Feature Barcode Technology for Cell Surface Protein (10x Genomics) following the manufacturer's instructions. The prepared libraries were quantified and quality checked using TapeStation (Agilent). The GEX libraries or hash-tag libraries from each group were combined to generate a pooled GEX library and a pooled hash-tag library, respectively. The pooled libraries were sequenced using NovaSeq X Plus (Illumina) with a depth of 2 billion reads for the pooled GEX library and 200 million reads for the pooled hash-tag library.

scRNA-seq data analysis

Alignments and count aggregation of gene expression and hash-tag reads were performed using the Cell Ranger Count v7.1.0 pipeline on

10x Cloud with the default settings. Gene expression reads or hash-tag reads were aligned to the mouse genome (mm10-2020-A) and the hash-tag sequence list, respectively. The quality control report showed that 10,209 or 1367 cells were detected for the *mo*PD-1^{WT} and *mo*PD-1^{huICD} sample, respectively. The downstream analyses were performed using the Scanpy toolkit (*65*). Cells were initially quality-filtered on the basis of the number of detected genes >200. Genes were quality-filtered on the basis of the expressing cells >3 and the read counts >0. Cells were quality-filtered on the basis of the percentage of mitochondrial reads <5% to remove dead cells, the total counts of gene reads <7500 to remove doublets, and the total counts of gene reads >500 to remove low-quality cells. After filtering, the transcript counts were normalized by using the scanpy.pp.normalize_total function with the default settings and transformed to a logarithmic scale by using the scanpy.pp.log1p function with the default settings. Cells were further filtered on the basis of the expression of *Cd3e* > 0 and *Cd8a* > 0 to select CD8$^+$ T cells, resulting in 7569 *mo*PD-1^{WT}–expressing cells and 952 *mo*PD-1^{huICD}–expressing cells.

For identifying the tumor origin of each cell, hash-tag reads were separated into two groups on the basis of their PD-1 ICD origins. The hash-tag reads in each group were processed using the scanpy.pp.pca function with n_comp = 3, the scanpy.pp.neighbors function with n_neighbors = 30, and the scanpy.tl.umap function to compute the principal components analysis (PCA) coordinates, the nearest neighbors distance matrix, and the UMAP. The cells were further clustered into subgroups using the scanpy.tl.leiden function with resolution = 0.45 or 0.5 for the *mo*PD-1^{WT} or *mo*PD-1^{huICD} group, and the hash-tag labels were manually annotated to each cell cluster.

For clustering of total P14 cells based on the gene expression, PCA coordinates of total cells were computed using the scanpy.pp.pca function with n_comps = 30, the nearest neighbors distance matrix was computed using the scanpy.pp.neighbors function with n_neighbors = 50, and the UMAP was computed using the scanpy.tl.umap function. The cells were further clustered into subgroups using the scanpy.tl.leiden function with resolution = 0.4. For analyzing *Tox*$^+$ P14 cells, the gene expression and hash-tag matrix data were filtered on the basis of the expression of *Tox* > 0, and the *Tox*$^+$ cells were clustered using the same method for total cells except that the Leiden resolution was set to 0.5.

For Fig. 5F and fig. S11D, the gene counts in each group were visualized using the scanpy.pl.violin function, and the false discovery rate (FDR) was calculated using the scanpy.tl.rank_genes_groups function with the method = "wilcoxon" setting. The dot plots in Fig. 5H and fig. S11E were generated using the scanpy.pl.dotplot function with the default settings. The % population in each cell cluster in Fig. 5I and fig. S11F was calculated by dividing the number of cells in each cluster by the total number of cells for each hash-tag sample. For computing the cell cycle phase shown in fig. S12, signature genes for cell cycle phase were derived from a previous study (*66*), and the score of each cell cluster was calculated using the scanpy.tl.score_genes_cell_cycle function with the default settings.

Proteins

Streptavidin (#S888) was purchased from Invitrogen. BSA (#A-420-1) was purchased from Goldbio. Recombinant protein *hu*PD-1–His (#10377-H08H), *hu*PD-L1–His (#10084-H08H), *mo*PD-1–His (#50124-M08H), *mo*PD-L1–His (#50010-M08H), *hu*ICAM-1 (#10346-H08H), and *mo*ICAM-1 (#50440-M08H) were purchased from SinoBiological. Recombinant protein *hu*PD-1^{ECD}-His (#PD1-H5221), *hu*PDL1^{ECD}-*hu*Fc (#PD1-H5258), *hu*PD-L2^{ECD}–*hu*Fc (#PD2-H5251), *mo*PD-1^{ECD}–His (#PD1-M5228), *mo*PD-L1^{ECD}–*hu*Fc (#PD1-M5251), and *mo*PD-L2^{ECD}–*hu*Fc (#PD2-M5254) were purchased from AcroBiosystems. His-tagged human Lck (amino acids 3 to 509) was expressed in the Bac-to-Bac baculovirus system and purified as previously described (*41*). All His-tagged PD-1^{ICD} were cloned into pET28A vector and expressed in the BL21(DE3) strain of *Escherichia coli*. The expressed proteins were captured by Ni-NTA agarose (Thermo Fisher Scientific), washed thrice with low-imidazole buffer (50 mM Hepes-NaOH, pH 8.0, 150 mM NaCl, 30 mM imidazole, and 7 mM β-mercaptoethanol), and eluted with high-imidazole buffer (50 mM Hepes-NaOH, pH 8.0, 150 mM NaCl, 500 mM imidazole, 50 mM Hepes-NaOH, pH 8.0, 150 mM NaCl, and 7 mM β-mercaptoethanol). The eluted proteins were gel filtered using a Superdex 75 Increase column (GE Healthcare) in storage buffer (50 mM Hepes-NaOH, pH 7.5, 150 mM NaCl, 1 mM TCEP, and 10% glycerol); monomeric fractions were pooled, snap frozen, and stored at −80°C until use. C-terminally SNAP-tag-fused Shp1^{tSH2} (amino acids 4 to 215) or Shp2^{tSH2} (amino acids 5 to 218) were each cloned into the pGEX-6P2 vector that encodes an N-terminal GST-tag followed by a preScission protease cleavage site (LEVLFQGP). The GST-fused proteins were expressed in the BL21(DE3) strain of *E. coli*, purified using Glutathione Agarose 4B (Gold Biotechnology), and eluted with preScission buffer [50 mM Hepes-NaOH, pH 7.5, 150 mM NaCl, 0.5 mM TCEP, and 3C protease (20 U/ml)] to remove the GST-tag. The eluted proteins were further gel filtered using a Superdex 200 Increase column (GE Healthcare) in storage buffer (50 mM Hepes-NaOH, pH 7.5, 150 mM NaCl, 1 mM TCEP, and 10% glycerol), and the monomeric fractions were pooled and stored at −80°C until use. The SNAP-tagged SH2 proteins used in the liposome reconstitution assay were labeled with Snap-Cell505 star and purified using Zeba Spin Desalting Columns (Thermo Fisher Scientific) following the manufacturer's instruction. The labeled proteins were snap frozen and stored at −80°C until use.

Coculture assays

For measuring IL-2 secretion and CD69 expression in Jurkat:Raji coculture assays in Figs. 1 and 2, Raji B cells expressing *hu*PD-L1 or *mo*PD-L1 were preincubated with the indicated concentration of SEE in the presence of the indicated concentration of atezolizumab at 37°C for 30 min. The preincubated Raji B cells were mixed with Jurkat cells expressing the indicated PD-1 variant in a 96-well plate and centrifuged at 300*g* for 1 min to initiate Jurkat:Raji contact. After incubating the cell mixtures at 37°C/5% CO_2 for 6 or 24 hours, the amount of IL-2 in the medium was quantified using the human IL-2 ELISA kit (BioLegend), or CD69 expression on Jurkat cells was measured by FACS. For measuring CD69 expression on Jurkat cells, Raji cells were stained with the ViaFluor 405 Cell Proliferation Kit (Biotium) before SEE-pulse. The Jurkat:Raji mixtures were stained with APC anti-human CD69, then analyzed on an LSRFortessa X-20 (BD). 405-SE positive cells were excluded in FACS data to specifically measure CD69 expression on Jurkat cells. The dose-response curve in Fig. 1B was fit using the "log(agonist) vs. response -- Variable slope" model using GraphPad Prism 5.0.

For measuring IL-2 secretion in the DO11.10:A20 coculture assay in Figs. 1 and 2, A20 cells expressing *hu*PD-L1 or *mo*PD-L1 were incubated with or without atezolizumab (120 μg/ml) at 37°C for 30 min, then mixed with the indicated concentration of $OVA_{323-339}$ in a 96-well plate. The treated A20 cells were further mixed with DO11.10 T cell hybridoma and centrifuged at 300*g* for 1 min. The

cell mixture was incubated at 37°C for 24 hours. The amount of IL-2 in the culture medium was measured using a mouse IL-2 ELISA kit (BioLegend).

For measuring IL-2 secretion in the human primary $CD4^+$ T:Raji coculture assay in Fig. 2, *CD80*$^{-/-}$ Raji B cells or *CD80*$^{-/-}$*GFPNb-TMD-TagBFP*$^+$–expressing Raji B cells were preincubated with SEB (0.5 μg/ml) at 37°C/5% CO_2 for 30 min. Human primary $CD4^+$ T cells were washed twice with fresh RPMI containing 10% FBS to remove IL-2, mixed with SEB-loaded Raji B cells in a round-bottom 96-well plate, and centrifuged at 300*g* for 1 min to initiate cell contact. The cell mixture was then incubated at 37°C/5% CO_2. After 12 hours, the amount of secreted IL-2 was quantified using the human IL-2 ELISA kit (BioLegend).

For measuring the Shp2-dependent PD-1 functions in fig. S6, the indicated human or mouse T cells were serum-starved for 24 hours, incubated with 0 or 30 μM SHP099 in a serum-free RPMI medium for 2 hours, and further incubated with anti–PD-1 blockade antibody (0 or 80 μg/ml; human: pembrolizumab, mouse: clone RMP1-14) for 30 min. To stimulate human T cells, *hu*PD-L1–expressing *PTPN11*$^{-/-}$ Raji cells were treated with SEB (0.5 μg/ml) for 30 min, mixed with SHP099-treated human T cells in a serum-free RPMI, and incubated for 6 hours. To stimulate mouse T cells, B16.gp33 cells were treated with mouse IFN-γ (100 U/ml) in the culture medium for 24 hours, washed with 1× PBS thrice, and incubated with SHP099-treated mouse T cells in a serum-free RPMI for 6 hours. The final concentrations of SHP099 were 0 or 5 μM in the T:APC mixtures. Secreted IL-2 in the supernatant was measured using human or mouse IL-2 ELISA kit (BioLegend). All incubations were performed at 37°C/5% CO_2. Percent inhibition on the T cell stimulation indicators, IL-2 secretion, and CD69 expression exerted by PD-1 variants were calculated using the following formula: 100% × [1 – (the readout value under no blockade condition)/(the readout value under each blockade concentration)].

For measuring the enrichment of PD-1 on Jurkat:Raji contact surfaces in Fig. 3, Raji cells expressing mCherry-tagged *hu*PD-L1 or *mo*PD-L1 were incubated with SEE (0.06 ng/ml) in the presence or absence of atezolizumab (120 μg/ml) at 37°C for 30 min. The treated Raji B cells were mixed with Jurkat cells expressing indicated mGFP-tagged PD-1 variants in a 96-well plate and centrifuged at 300*g* for 1 min to initiate cell contact. The cell mixtures were incubated at 37°C for 2 min, fixed with 4% PFA at room temperature (RT) for 15 min, washed with PBS containing 2% FBS, and transferred into a glass-bottom 96-well plate (Cellvis). Cell images were acquired using a confocal microscope (Nikon, Ti2-E).

Liposome reconstitution assay

The liposome reconstitution assay was performed as described with modifications (*41*). Briefly, large unilamellar liposomes (lipid compositions: 89.7% POPC, 10% DGS-NTA-Ni, 0.3% rhodamine-PE; diameter: 200 nm) prepared as previously described (*41*) were attached with 50 nM His-tagged Lck and the indicated concentration of His-tagged PD-1^{ICD} and further mixed with 50 nM SC505-labeled Shp2^{tSH2}. The liposome-protein mixture was incubated at RT for 40 min with continuous monitoring of the F.I. of SC505 to establish a baseline and then added with 1 mM ATP, after which the F.I. of SC505 was monitored for an additional 60 min. The F.I. of SC505 at 30 min after ATP addition was used to measure the K_d of Shp2^{tSH2} binding to each PD-1^{ICD} variant. The binding curves in Fig. 4H and fig. S8B were fit using the "On site—Specific binding" model using GraphPad Prism 5.0.

LUV-SLB binding assay

SLBs were prepared as described, with modifications (*28*). A 96-well glass-bottom plate (Cellvis) was incubated with 2.5% Hellmanex at 50°C overnight and washed extensively with ddH_2O. Glass-bottom wells were etched with 6 N NaOH at 50°C for 90 min and washed with ddH_2O and Hepes-buffered saline (HBS: 50 mM Hepes-NaOH, pH 7.5, and 150 mM NaCl). Small unilamellar vesicles (lipid compositions: 95.9% POPC, 2% Biotinyl-PE, 2% DGS-NTA-Ni, and 0.1% PEG5k-PE), prepared via a freeze-thaw method as previously described (*67*), were mixed with DiD (1 μg/ml), added to the washed wells containing HBS, and incubated at 50°C for 90 min and further at room temperature for 30 min to form stable SLBs. Subsequently, the wells were rinsed with HBS containing BSA (1 mg/ml) to block the SLBs and incubated with 3 nM *hu*PD-L1–His or *mo*PD-L1–His at RT for 1 hour before being washed with HBS containing BSA (1 mg/ml). LUVs (lipid compositions: 89.7% POPC, 10% DGS-NTA-Ni, and 0.3% Bodipy-PE) were prepared as described above. LUVs (total lipid concentration: 0.17 mM) were incubated with 0.83 nM *hu*PD-1–His or *mo*PD-1–His at RT for 1 hour, allowing each LUV to capture about five PD-1–His molecules. The PD-L1–attached SLBs were then incubated with PD-1–attached LUVs (total lipid concentration: 70 μM) at RT for 30 min and subjected to TIRF-M.

Cell-SLB assay

SLBs were prepared as described above. After SLB formation, the wells were rinsed with PBS containing BSA (1 mg/ml) to block the SLBs, then incubated with streptavidin (1 mg/ml), 3 nM *hu*ICAM1-His, and indicated concentrations of *hu*PD-L1–His or *mo*PD-L1–His at RT for 1 hour. For preparing SLBs for DO11.10 T cell hybridoma, *hu*ICAM1-His was replaced with the same concentration of *mo*ICAM1-His. The SLBs were then rinsed with PBS containing BSA (1 mg/ml) to remove unbound proteins and further incubated with biotin anti-*hu*CD3ε (2 μg/ml) at RT for 30 min. The functionalized SLBs were washed with 1× PBS containing BSA (1 mg/ml) and 1× imaging buffer (20 mM Hepes-NaOH, pH 7.5, 137 mM NaCl, 5 mM KCl, 1 mM $CaCl_2$, 2 mM $MgCl_2$, 0.7 mM Na_2HPO_4, and 6 mM D-glucose) and incubated at 37°C for 15 min before the addition of cells. Cells were resuspended in 1× imaging buffer, loaded onto SLBs, and incubated at 37°C for 10 min. After incubation, cells were fixed with 2% PFA at RT for 10 min and washed with PBS containing BSA (1 mg/ml). The fixed cells were further permeabilized with 0.1% saponin at RT for 30 min. For observing endogenous Shp2, the fixed and permeabilized cells were incubated with anti-Shp2*AF647 at 4°C overnight, washed with 1× PBS, and fixed with 4% PFA. TIRF images were acquired on a Nikon Eclipse Ti microscope equipped with a 100× Apo TIRF 1.49 NA (numerical aperture) objective lens, controlled by the Micro-Manager (*68*). The dose-response curve in Fig. 3F was fit using the "log(agonist) vs. response -- Variable slope" model using GraphPad Prism 5.0.

BLI assays

BLI assays were performed on Octet R8 (Sartorius) using the anti-human IgG Fc Capture (AHC) biosensor. AHC sensors were presoaked in 1× PBS for 30 min and incubated with *hu*PD-L1^{ECD}-*hu*Fc or *hu*PD-L2^{ECD}-*hu*Fc (5 μg/ml), or *mo*PD-L1^{ECD}-*hu*Fc or *mo*PD-L2^{ECD}-*hu*Fc (10 μg/ml) diluted in kinetic buffer (1× PBS with 0.02% Tween 20, 0.1% BSA, and 50 μM EDTA) for 300 s. Analyte protein *hu*PD-1^{ECD}-His or *mo*PD-1^{ECD}-His was diluted in a twofold series

in kinetic buffer (0.15625, 0.3125, 0.625, 1.25, 2.5, 5, and 10 μM). Ligand-coated AHC sensors were dipped into diluted PD-1 proteins for 180 s for association and subsequently dipped into kinetic buffer for 180 s for dissociation. The generated data were fitted to a 1:1 kinetic model using the Octet Analysis Studio (Sartorius, ver. 12.2.2.26) to estimate K_d values.

Image analysis

All image analyses were conducted using Fiji (*69*). PD-1 enrichment shown in Fig. 3C was calculated by dividing the PD-1 F.I. within the Jurkat:Raji contact zone by the PD-1 F.I. outside the contact zone. The cluster indices in Fig. 3 (E and F) were calculated by dividing the F.I. of clustered PD-1 by the F.I. of total PD-1 signal. For measuring the F.I. of clustered PD-1, TIRF images were subjected to the "subtract background" function with the "rolling ball radius" set as 20 pixels to define the PD-1 microclusters. The whole F.I.s of raw images were measured as the F.I. of total PD-1. For calculating the Shp2 binding to PD-1 microclusters shown in Figs. 4 and 6, the F.I.s of PD-1 and anti-Shp2 on PD-1 microclusters were used. The green (PD-1) and far-red (anti-Shp2) or red (mCherry-Shp2) channels of TIRF images were subjected to the subtract background function with the same setting described above, and the binary, processed green channel images were used to define the positions of PD-1 microclusters. The background-subtracted images were masked with the binary PD-1 microcluster images, and the F.I.s of the masked green, far-red, and red channels were measured for PD-1, anti-Shp2, or mCherry-Shp2 F.I.

Phylogenies and orthologous coding sequences of genes

Phylogenies in Fig. 6A, the inference of positive selection and relaxation, and ASR were obtained from TimeTree5 (*70*) by querying with the species needed. Branch lengths in Fig. 6A were obtained from TimeTree as well. The orthologous coding sequences of respective genes were obtained from OrthoMaM v12a (*71*) for all mammal species. Nonmammal orthologs of PD-1 were obtained from NCBI Orthologs for Gene ID 5133. PD-1 sequences of *Xenopus tropicalis* (accession no. A0A803JYL7), *Xenopus laevis* (accession no. A0A1L8G9Q9), *Alligator sinensis* (accession no. A0A3Q0GJP7), and *Alligator mississippiensis* (accession no. A0A151MMB5) were obtained from UniProt. For obtaining the states of the PD-1 pre-ITSM sequences in Fig. 6A, we first aligned all PD-1 orthologs by linsi algorithm in MAFFT v7.310 (*72*) and then manually checked the validity of alignment and the states of pre-ITSM sequence. For (i) the inference of positive selection and relaxation in PD-1 and related genes and (ii) the ASR of PD-1, the corresponding coding sequence alignment of the gene was first retrieved from the OrthoMaM database and then filtered as follows. We removed gap-rich sequences by simultaneously requiring the alignment to (i) contain no fewer than five rodent species and to (ii) contain no sequence with more than 10% gaps. If the two requirements cannot be satisfied, we increased the gap proportion requirement by 5% increments in (ii) until both criteria were met. We then removed the sites that contain only gaps in all remaining species in the alignment and used the derived alignment for downstream analyses.

Statistical tests of positive selection and relaxation in sequence data

The existence of positive selection and relaxation in sequence evolution was tested by the BUSTED and the RELAX program in the HYPHY package v2.5.8 (*48*, *49*). For each gene to be tested, the filtered alignment and the corresponding tree topology were used as input. In both BUSTED and RELAX, we assigned foreground branches in the tree according to the following two scenarios: (i) the MRCA branch of the clade of species (all rodents or all primates) and (ii) all branches in the clade (i.e., the subtree under the MRCA branch) excluding the MRCA branch. All other parameters were set as default in the analyses. BUSTED conducts a likelihood ratio test on whether a proportion of the foreground branch(es) experienced positive selection (branch-site test). RELAX conducts a likelihood ratio test on whether selection intensity k on the foreground branch(es) is the same ($k = 1$) as the background branches (all other branches by default). Intensification and relaxation of selection corresponds to the cases in which k increases ($k > 1$) or decreases ($k < 1$).

Ancestral sequence reconstruction

We followed common practices to conduct the ASR analysis by using the computational pipeline Lazarus (retrieved from https://github.com/cxhernandez/project-lazarus) (*73*). We started from two 107-species filtered sequence alignments, containing the amino acid and codon sequences for PD-1, respectively. Together with the 107-species tree topology as input, we first inferred the best-fit evolutionary parameters (branch lengths and substitution model) separately for the amino acid sequence alignment and the codon sequence alignment by IQTREE v1.6.12, constraining the best-fit substitution matrix to be chosen from JTT, WAG, or LG. We then ran the Lazarus pipeline separately using the amino acid sequence alignment and the codon sequence alignment, together with the trees containing respective branch lengths as input. The other Lazarus command-line parameters were set as "--model jones.dat --asrv 4 --alpha 1 --codeml --gapcorrect --branch_lengths 'fixed.'" The "--outgroup" was set as all species in the tree excluding rodents. Lazarus called PAML v4 (*74*) for maximum likelihood ancestral state inference and then assigned gaps at individual sites in the alignment when necessary according to maximum parsimony. As a result, we obtained an ASR for amino acid sequences and another ASR for codon sequences. We compared the reconstructed codon and amino acid states at each site. For sites with inconsistent amino acid and codon ASR states, when the codon states were not parsimonious in terms of their translated amino acid states, we modified the codon states according to the corresponding reconstructed amino acid states and maximum parsimony rules. For the pre-ITSM sequence, we first manually assigned the maximum parsimony amino acid states or gaps for the three sites at each node and then assigned the codon states where a nongap amino acid state was assigned, according to the Lazarus output codon ASR result. The reconstructed sequences were then used for downstream experiments.

Statistics

Data are shown as mean ± SD, ± SEM, or violin box plots as indicated in the figure legends. The number of replicates is indicated in the figure legends. Statistical significance was evaluated by unpaired two-tailed Student's t test, one-way analysis of variance (ANOVA), two-way ANOVA, or Wilcoxon signed-rank test as indicated in the figure legends. All statistical analyses were performed using GraphPad Prism 5, unless stated in the figure legends. Data with P values <0.05 were considered statistically significant.

Supplementary Materials

The PDF file includes:

Figs. S1 to S14
Tables S1 and S2
Legends for movies S1 and S2
Legend for data S3

Other Supplementary Material for this manuscript includes the following:

Movies S1 and S2
Data S3
MDAR Reproducibility Checklist

REFERENCES AND NOTES

1. L. M. Francisco, P. T. Sage, A. H. Sharpe, The PD-1 pathway in tolerance and autoimmunity. *Immunol. Rev.* **236**, 219–242 (2010).
2. H. Dong, S. E. Strome, D. R. Salomao, H. Tamura, F. Hirano, D. B. Flies, P. C. Roche, J. Lu, G. Zhu, K. Tamada, V. A. Lennon, E. Celis, L. Chen, Tumor-associated B7-H1 promotes T-cell apoptosis: A potential mechanism of immune evasion. *Nat. Med.* **8**, 793–800 (2002).
3. W. Zou, J. D. Wolchok, L. Chen, PD-L1 (B7-H1) and PD-1 pathway blockade for cancer therapy: Mechanisms, response biomarkers, and combinations. *Sci. Transl. Med.* **8**, 328rv324 (2016).
4. A. H. Sharpe, E. J. Wherry, R. Ahmed, G. J. Freeman, The function of programmed cell death 1 and its ligands in regulating autoimmunity and infection. *Nat. Immunol.* **8**, 239–245 (2007).
5. L. Chen, Co-inhibitory molecules of the B7-CD28 family in the control of T-cell immunity. *Nat. Rev. Immunol.* **4**, 336–347 (2004).
6. D. R. Leach, M. F. Krummel, J. P. Allison, Enhancement of antitumor immunity by CTLA-4 blockade. *Science* **271**, 1734–1736 (1996).
7. J. Mestas, C. C. Hughes, Of mice and not men: Differences between mouse and human immunology. *J. Immunol.* **172**, 2731–2738 (2004).
8. L. K. Beura, S. E. Hamilton, K. Bi, J. M. Schenkel, O. A. Odumade, K. A. Casey, E. A. Thompson, K. A. Fraser, P. C. Rosato, A. Filali-Mouhim, R. P. Sekaly, M. K. Jenkins, V. Vezys, W. N. Haining, S. C. Jameson, D. Masopust, Normalizing the environment recapitulates adult human immune traits in laboratory mice. *Nature* **532**, 512–516 (2016).
9. K. Medetgul-Ernar, M. M. Davis, Standing on the shoulders of mice. *Immunity* **55**, 1343–1353 (2022).
10. M. F. Sanmamed, C. Chester, I. Melero, H. Kohrt, Defining the optimal murine models to investigate immune checkpoint blockers and their combination with other immunotherapies. *Ann. Oncol.* **27**, 1190–1198 (2016).
11. R. Goodwin, G. Giaccone, H. Calvert, M. Lobbezoo, E. A. Eisenhauer, Targeted agents: How to select the winners in preclinical and early clinical studies? *Eur. J. Cancer* **48**, 170–178 (2012).
12. A. Gunjur, A. Balasubramanian, U. Hafeez, S. Menon, L. Cher, S. Parakh, H. K. Gan, Poor correlation between preclinical and patient efficacy data for tumor targeted monotherapies in glioblastoma: The results of a systematic review. *J. Neurooncol.* **159**, 539–549 (2022).
13. J. T. Atkins, G. C. George, K. Hess, K. L. Marcelo-Lewis, Y. Yuan, G. Borthakur, S. Khozin, P. LoRusso, D. S. Hong, Pre-clinical animal models are poor predictors of human toxicities in phase 1 oncology clinical trials. *Br. J. Cancer* **123**, 1496–1501 (2020).
14. N. L. Bayless, J. A. Bluestone, S. Bucktrout, L. H. Butterfield, E. M. Jaffee, C. A. Koch, B. O. Roep, A. H. Sharpe, W. J. Murphy, A. C. Villani, T. L. Walunas, Development of preclinical and clinical models for immune-related adverse events following checkpoint immunotherapy: A perspective from SITC and AACR. *J. Immunother. Cancer* **9**, e002627 (2021).
15. Y. Ishida, Y. Agata, K. Shibahara, T. Honjo, Induced expression of PD-1, a novel member of the immunoglobulin gene superfamily, upon programmed cell death. *EMBO J.* **11**, 3887–3895 (1992).
16. G. J. Freeman, A. J. Long, Y. Iwai, K. Bourque, T. Chernova, H. Nishimura, L. J. Fitz, N. Malenkovich, T. Okazaki, M. C. Byrne, H. F. Horton, L. Fouser, L. Carter, V. Ling, M. R. Bowman, B. M. Carreno, M. Collins, C. R. Wood, T. Honjo, Engagement of the PD-1 immunoinhibitory receptor by a novel B7 family member leads to negative regulation of lymphocyte activation. *J. Exp. Med.* **192**, 1027–1034 (2000).
17. D. L. Barber, E. J. Wherry, D. Masopust, B. Zhu, J. P. Allison, A. H. Sharpe, G. J. Freeman, R. Ahmed, Restoring function in exhausted CD8 T cells during chronic viral infection. *Nature* **439**, 682–687 (2006).
18. M. Ogishi, R. Yang, C. Aytekin, D. Langlais, M. Bourgey, T. Khan, F. A. Ali, M. Rahman, O. M. Delmonte, M. Chrabieh, P. Zhang, C. Gruber, S. J. Pelham, A. N. Spaan, J. Rosain, W. T. Lei, S. Drutman, M. D. Hellmann, M. K. Callahan, M. Adamow, P. Wong, J. D. Wolchok, G. Rao, C. S. Ma, Y. Nakajima, T. Yaguchi, K. Chamoto, S. C. Williams, J. F. Emile, F. Rozenberg, M. S. Glickman, F. Rapaport, G. Kerner, G. Allington, I. Tezcan, D. Cagdas, F. O. Hosnut, F. Dogu, A. Ikinciogullari, V. K. Rao, L. Kainulainen, V. Beziat, J. Bustamante, S. Vilarinho, R. P. Lifton, B. Boisson, L. Abel, D. Bogunovic, N. Marr, L. D. Notarangelo, S. G. Tangye, T. Honjo, P. Gros, S. Boisson-Dupuis, J. L. Casanova, Inherited PD-1 deficiency underlies tuberculosis and autoimmunity in a child. *Nat. Med.* **27**, 1646–1654 (2021).
19. S. L. Topalian, C. G. Drake, D. M. Pardoll, Immune checkpoint blockade: A common denominator approach to cancer therapy. *Cancer Cell* **27**, 450–461 (2015).
20. D. M. Pardoll, The blockade of immune checkpoints in cancer immunotherapy. *Nat. Rev. Cancer* **12**, 252–264 (2012).
21. P. Sharma, S. Hu-Lieskovan, J. A. Wargo, A. Ribas, Primary, adaptive, and acquired resistance to cancer immunotherapy. *Cell* **168**, 707–723 (2017).
22. P. Sharma, J. P. Allison, Immune checkpoint targeting in cancer therapy: Toward combination strategies with curative potential. *Cell* **161**, 205–214 (2015).
23. A. Ribas, J. D. Wolchok, Cancer immunotherapy using checkpoint blockade. *Science* **359**, 1350–1355 (2018).
24. G. J. Freeman, Structures of PD-1 with its ligands: Sideways and dancing cheek to cheek. *Proc. Natl. Acad. Sci. U.S.A.* **105**, 10275–10276 (2008).
25. E. Lazar-Molnar, Q. Yan, E. Cao, U. Ramagopal, S. G. Nathenson, S. C. Almo, Crystal structure of the complex between programmed death-1 (PD-1) and its ligand PD-L2. *Proc. Natl. Acad. Sci. U.S.A.* **105**, 10483–10488 (2008).
26. D. Y. Lin, Y. Tanaka, M. Iwasaki, A. G. Gittis, H. P. Su, B. Mikami, T. Okazaki, T. Honjo, N. Minato, D. N. Garboczi, The PD-1/PD-L1 complex resembles the antigen-binding Fv domains of antibodies and T cell receptors. *Proc. Natl. Acad. Sci. U.S.A.* **105**, 3011–3016 (2008).
27. T. Yokosuka, M. Takamatsu, W. Kobayashi-Imanishi, A. Hashimoto-Tane, M. Azuma, T. Saito, Programmed cell death 1 forms negative costimulatory microclusters that directly inhibit T cell receptor signaling by recruiting phosphatase SHP2. *J. Exp. Med.* **209**, 1201–1217 (2012).
28. E. Hui, J. Cheung, J. Zhu, X. Su, M. J. Taylor, H. A. Wallweber, D. K. Sasmal, J. Huang, J. M. Kim, I. Mellman, R. D. Vale, T cell costimulatory receptor CD28 is a primary target for PD-1-mediated inhibition. *Science* **355**, 1428–1433 (2017).
29. B. Wang, W. Zhang, V. Jankovic, J. Golubov, P. Poon, E. M. Oswald, C. Gurer, J. Wei, I. Ramos, Q. Wu, J. Waite, M. Ni, C. Adler, Y. Wei, L. Macdonald, T. Rowlands, S. Brydges, J. Siao, W. Poueymirou, D. MacDonald, G. D. Yancopoulos, M. A. Sleeman, A. J. Murphy, D. Skokos, Combination cancer immunotherapy targeting PD-1 and GITR can rescue $CD8^+$ T cell dysfunction and maintain memory phenotype. *Sci. Immunol.* **3**, eaat7061 (2018).
30. E. A. Philips, J. Liu, A. Kvalvaag, A. M. Morch, A. S. Tocheva, C. Ng, H. Liang, I. M. Ahearn, R. Pan, C. C. Luo, A. Leithner, Z. Qin, Y. Zhou, A. Garcia-Espana, A. Mor, D. R. Littman, M. L. Dustin, J. Wang, X. P. Kong, Transmembrane domain-driven PD-1 dimers mediate T cell inhibition. *Sci. Immunol.* **9**, eade6256 (2024).
31. J. L. Riley, PD-1 signaling in primary T cells. *Immunol. Rev.* **229**, 114–125 (2009).
32. A. Chaudhri, Y. Xiao, A. N. Klee, X. Wang, B. Zhu, G. J. Freeman, PD-L1 binds to B7-1 only in cis on the same cell surface. *Cancer Immunol. Res.* **6**, 921–929 (2018).
33. D. Sugiura, T. Maruhashi, I. M. Okazaki, K. Shimizu, T. K. Maeda, T. Takemoto, T. Okazaki, Restriction of PD-1 function by cis-PD-L1/CD80 interactions is required for optimal T cell responses. *Science* **364**, 558–566 (2019).
34. Y. Zhao, C. K. Lee, C. H. Lin, R. B. Gassen, X. Xu, Z. Huang, C. Xiao, C. Bonorino, L. F. Lu, J. D. Bui, E. Hui, PD-L1:CD80 cis-heterodimer triggers the co-stimulatory receptor CD28 while repressing the inhibitory PD-1 and CTLA-4 pathways. *Immunity* **51**, 1059–1073.e9 (2019).
35. S. A. Oh, D. C. Wu, J. Cheung, A. Navarro, H. Xiong, R. Cubas, K. Totpal, H. Chiu, Y. Wu, L. Comps-Agrar, A. M. Leader, M. Merad, M. Roose-Germa, S. Warming, M. Yan, J. M. Kim, S. Rutz, I. Mellman, PD-L1 expression by dendritic cells is a key regulator of T-cell immunity in cancer. *Nat Cancer* **1**, 681–691 (2020).
36. K. Magiera-Mularz, J. Kocik, B. Musielak, J. Plewka, D. Sala, M. Machula, P. Grudnik, M. Hajduk, M. Czepiel, M. Siedlar, T. A. Holak, L. Skalniak, Human and mouse PD-L1: Similar molecular structure, but different druggability profiles. *iScience* **24**, 101960 (2021).
37. X. Cheng, V. Veverka, A. Radhakrishnan, L. C. Waters, F. W. Muskett, S. H. Morgan, J. Huo, C. Yu, E. J. Evans, A. J. Leslie, M. Griffiths, C. Stubberfield, R. Griffin, A. J. Henry, A. Jansson, J. E. Ladbury, S. Ikemizu, M. D. Carr, S. J. Davis, Structure and interactions of the human programmed cell death 1 receptor. *J. Biol. Chem.* **288**, 11771–11785 (2013).
38. Y. Zhao, D. L. Harrison, Y. Song, J. Ji, J. Huang, E. Hui, Antigen-presenting cell-intrinsic PD-1 neutralizes PD-L1 in cis to attenuate PD-1 signaling in T cells. *Cell Rep.* **24**, 379–390.e6 (2018).
39. T. Okazaki, A. Maeda, H. Nishimura, T. Kurosaki, T. Honjo, PD-1 immunoreceptor inhibits B cell receptor-mediated signaling by recruiting src homology 2-domain-containing tyrosine phosphatase 2 to phosphotyrosine. *Proc. Natl. Acad. Sci. U.S.A.* **98**, 13866–13871 (2001).
40. Y. N. Chen, M. J. LaMarche, H. M. Chan, P. Fekkes, J. Garcia-Fortanet, M. G. Acker, B. Antonakos, C. H. Chen, Z. Chen, V. G. Cooke, J. R. Dobson, Z. Deng, F. Fei, B. Firestone, M. Fodor, C. Fridrich, H. Gao, D. Grunenfelder, H. X. Hao, J. Jacob, S. Ho, K. Hsiao, Z. B. Kang, R. Karki, M. Kato, J. Larrow, L. R. La Bonte, F. Lenoir, G. Liu, S. Liu, D. Majumdar, M. J. Meyer, M. Palermo, L. Perez, M. Pu, E. Price, C. Quinn, S. Shakya, M. D. Shultz, J. Slisz, K. Venkatesan, P. Wang, M. Warmuth, S. Williams, G. Yang, J. Yuan, J. H. Zhang, P. Zhu, T. Ramsey, N. J. Keen, W. R. Sellers, T. Stams, P. D. Fortin, Allosteric inhibition of SHP2 phosphatase inhibits cancers driven by receptor tyrosine kinases. *Nature* **535**, 148–152 (2016).

41. E. Hui, R. D. Vale, In vitro membrane reconstitution of the T-cell receptor proximal signaling network. *Nat. Struct. Mol. Biol.* **21**, 133–142 (2014).
42. J. Celis-Gutierrez, P. Blattmann, Y. Zhai, N. Jarmuzynski, K. Ruminski, C. Gregoire, Y. Ounoughene, F. Fiore, R. Aebersold, R. Roncagalli, M. Gstaiger, B. Malissen, Quantitative interactomics in primary T cells provides a rationale for concomitant PD-1 and BTLA coinhibitor blockade in cancer immunotherapy. *Cell Rep.* **27**, 3315–3330.e7 (2019).
43. P. Zhou, H. Shi, H. Huang, X. Sun, S. Yuan, N. M. Chapman, J. P. Connelly, S. A. Lim, J. Saravia, A. Kc, S. M. Pruett-Miller, H. Chi, Single-cell CRISPR screens in vivo map T cell fate regulomes in cancer. *Nature* **624**, 154–163 (2023).
44. I. Siddiqui, K. Schaeuble, V. Chennupati, S. A. Fuertes Marraco, S. Calderon-Copete, D. Pais Ferreira, S. J. Carmona, L. Scarpellino, D. Gfeller, S. Pradervand, S. A. Luther, D. E. Speiser, W. Held, Intratumoral Tcf1+PD-1+CD8+ T cells with stem-like properties promote tumor control in response to vaccination and checkpoint blockade immunotherapy. *Immunity* **50**, 195–211.e10 (2019).
45. S. J. Im, M. Hashimoto, M. Y. Gerner, J. Lee, H. T. Kissick, M. C. Burger, Q. Shan, J. S. Hale, T. H. Nasti, A. H. Sharpe, G. J. Freeman, R. N. Germain, H. I. Nakaya, H. H. Xue, R. Ahmed, Defining $CD8^+$ T cells that provide the proliferative burst after PD-1 therapy. *Nature* **537**, 417–421 (2016).
46. R. He, S. Hou, C. Liu, A. Zhang, Q. Bai, M. Han, Y. Yang, G. Wei, T. Shen, X. Yang, L. Xu, X. Chen, Y. Hao, P. Wang, C. Zhu, J. Ou, H. Liang, T. Ni, X. Zhang, X. Zhou, K. Deng, Y. Chen, Y. Luo, J. Xu, H. Qi, Y. Wu, L. Ye, Follicular CXCR5-expressing $CD8^+$ T cells curtail chronic viral infection. *Nature* **537**, 412–416 (2016).
47. B. C. Miller, D. R. Sen, R. Al Abosy, K. Bi, Y. V. Virkud, M. W. LaFleur, K. B. Yates, A. Lako, K. Felt, G. S. Naik, M. Manos, E. Gjini, J. R. Kuchroo, J. J. Ishizuka, J. L. Collier, G. K. Griffin, S. Maleri, D. E. Comstock, S. A. Weiss, F. D. Brown, A. Panda, M. D. Zimmer, R. T. Manguso, F. S. Hodi, S. J. Rodig, A. H. Sharpe, W. N. Haining, Subsets of exhausted $CD8^+$ T cells differentially mediate tumor control and respond to checkpoint blockade. *Nat. Immunol.* **20**, 326–336 (2019).
48. B. Murrell, S. Weaver, M. D. Smith, J. O. Wertheim, S. Murrell, A. Aylward, K. Eren, T. Pollner, D. P. Martin, D. M. Smith, K. Scheffler, S. L. Kosakovsky Pond, Gene-wide identification of episodic selection. *Mol. Biol. Evol.* **32**, 1365–1371 (2015).
49. J. O. Wertheim, B. Murrell, M. D. Smith, S. L. Kosakovsky Pond, K. Scheffler, RELAX: Detecting relaxed selection in a phylogenetic framework. *Mol. Biol. Evol.* **32**, 820–832 (2015).
50. V. C. Xie, J. Pu, B. P. Metzger, J. W. Thornton, B. C. Dickinson, Contingency and chance erase necessity in the experimental evolution of ancestral proteins. *eLife* **10**, e67336 (2021).
51. G. C. Finnigan, V. Hanson-Smith, T. H. Stevens, J. W. Thornton, Evolution of increased complexity in a molecular machine. *Nature* **481**, 360–364 (2012).
52. N. M. Foley, V. C. Mason, A. J. Harris, K. R. Bredemeyer, J. Damas, H. A. Lewin, E. Eizirik, J. Gatesy, E. K. Karlsson, K. Lindblad-Toh, Zoonomia Consortium, M. S. Springer, W. J. Murphy, A genomic timescale for placental mammal evolution. *Science* **380**, eabl8189 (2023).
53. S. Alvarez-Carretero, A. U. Tamuri, M. Battini, F. F. Nascimento, E. Carlisle, R. J. Asher, Z. Yang, P. C. J. Donoghue, M. Dos Reis, A species-level timeline of mammal evolution integrating phylogenomic data. *Nature* **602**, 263–267 (2022).
54. B. T. Fife, K. E. Pauken, The role of the PD-1 pathway in autoimmunity and peripheral tolerance. *Ann. N. Y. Acad. Sci.* **1217**, 45–59 (2011).
55. F. Martins, L. Sofiya, G. P. Sykiotis, F. Lamine, M. Maillard, M. Fraga, K. Shabafrouz, C. Ribi, A. Cairoli, Y. Guex-Crosier, T. Kuntzer, O. Michielin, S. Peters, G. Coukos, F. Spertini, J. A. Thompson, M. Obeid, Adverse effects of immune-checkpoint inhibitors: Epidemiology, management and surveillance. *Nat. Rev. Clin. Oncol.* **16**, 563–580 (2019).
56. G. Myers, Immune-related adverse events of immune checkpoint inhibitors: A brief review. *Curr. Oncol.* **25**, 342–347 (2018).
57. K. Adam, A. Iuga, A. S. Tocheva, A. Mor, A novel mouse model for checkpoint inhibitor-induced adverse events. *PLOS ONE* **16**, e0246168 (2021).
58. H. Nishimura, M. Nose, H. Hiai, N. Minato, T. Honjo, Development of lupus-like autoimmune diseases by disruption of the PD-1 gene encoding an ITIM motif-carrying immunoreceptor. *Immunity* **11**, 141–151 (1999).
59. H. Nishimura, T. Okazaki, Y. Tanaka, K. Nakatani, M. Hara, A. Matsumori, S. Sasayama, A. Mizoguchi, H. Hiai, N. Minato, T. Honjo, Autoimmune dilated cardiomyopathy in PD-1 receptor-deficient mice. *Science* **291**, 319–322 (2001).
60. T. Yokosuka, W. Kobayashi, K. Sakata-Sogawa, M. Takamatsu, A. Hashimoto-Tane, M. L. Dustin, M. Tokunaga, T. Saito, Spatiotemporal regulation of T cell costimulation by TCR-CD28 microclusters and protein kinase C theta translocation. *Immunity* **29**, 589–601 (2008).
61. M. A. Mintz, J. H. Felce, M. Y. Chou, V. Mayya, Y. Xu, J. W. Shui, J. An, Z. Li, A. Marson, T. Okada, C. F. Ware, M. Kronenberg, M. L. Dustin, J. G. Cyster, The HVEM-BTLA axis restrains T cell help to germinal center B cells and functions as a cell-extrinsic suppressor in lymphomagenesis. *Immunity* **51**, 310–323.e7 (2019).
62. U. Lorenz, SHP-1 and SHP-2 in T cells: Two phosphatases functioning at many levels. *Immunol. Rev.* **228**, 342–359 (2009).
63. M. Marasco, A. Berteotti, J. Weyershaeuser, N. Thorausch, J. Sikorska, J. Krausze, H. J. Brandt, J. Kirkpatrick, P. Rios, W. W. Schamel, M. Kohn, T. Carlomagno, Molecular mechanism of SHP2 activation by PD-1 stimulation. *Sci. Adv.* **6**, eaay4458 (2020).
64. D. Conant, T. Hsiau, N. Rossi, J. Oki, T. Maures, K. Waite, J. Yang, S. Joshi, R. Kelso, K. Holden, B. L. Enzmann, R. Stoner, Inference of CRISPR edits from sanger trace data. *CRISPR J.* **5**, 123–130 (2022).
65. F. A. Wolf, P. Angerer, F. J. Theis, SCANPY: Large-scale single-cell gene expression data analysis. *Genome. Biol.* **19**, 15 (2018).
66. I. Tirosh, B. Izar, S. M. Prakadan, M. H. Wadsworth, D. Treacy, J. J. Trombetta, A. Rotem, C. Rodman, C. Lian, G. Murphy, M. Fallahi-Sichani, K. Dutton-Regester, J. R. Lin, O. Cohen, P. Shah, D. Lu, A. S. Genshaft, T. K. Hughes, C. G. Ziegler, S. W. Kazer, A. Gaillard, K. E. Kolb, A. C. Villani, C. M. Johannessen, A. Y. Andreev, E. M. Van Allen, M. Bertagnolli, P. K. Sorger, R. J. Sullivan, K. T. Flaherty, D. T. Frederick, J. Jané-Valbuena, C. H. Yoon, O. Rozenblatt-Rosen, A. K. Shalek, A. Regev, L. A. Garraway, Dissecting the multicellular ecosystem of metastatic melanoma by single-cell RNA-seq. *Science* **352**, 189–196 (2016).
67. X. Su, J. A. Ditlev, M. K. Rosen, R. D. Vale, Reconstitution of TCR signaling using supported lipid bilayers. *Methods Mol. Biol.* **1584**, 65–76 (2017).
68. A. D. Edelstein, M. A. Tsuchida, N. Amodaj, H. Pinkard, R. D. Vale, N. Stuurman, Advanced methods of microscope control using muManager software. *J. Biol. Methods* **1**, e10 (2014).
69. J. Schindelin, I. Arganda-Carreras, E. Frise, V. Kaynig, M. Longair, T. Pietzsch, S. Preibisch, C. Rueden, S. Saalfeld, B. Schmid, J. Y. Tinevez, D. J. White, V. Hartenstein, K. Eliceiri, P. Tomancak, A. Cardona, Fiji: An open-source platform for biological-image analysis. *Nat. Methods* **9**, 676–682 (2012).
70. S. Kumar, M. Suleski, J. M. Craig, A. E. Kasprowicz, M. Sanderford, M. Li, G. Stecher, S. B. Hedges, TimeTree 5: An expanded resource for species divergence times. *Mol. Biol. Evol.* **39**, msac174 (2022).
71. R. Allio, F. Delsuc, K. Belkhir, E. J. P. Douzery, V. Ranwez, C. Scornavacca, OrthoMaM v12: A database of curated single-copy ortholog alignments and trees to study mammalian evolutionary genomics. *Nucleic Acids Res.* **52**, D529–D535 (2024).
72. K. Katoh, D. M. Standley, MAFFT multiple sequence alignment software version 7: Improvements in performance and usability. *Mol. Biol. Evol.* **30**, 772–780 (2013).
73. V. Hanson-Smith, B. Kolaczkowski, J. W. Thornton, Robustness of ancestral sequence reconstruction to phylogenetic uncertainty. *Mol. Biol. Evol.* **27**, 1988–1999 (2010).
74. Z. Yang, PAML 4: Phylogenetic analysis by maximum likelihood. *Mol. Biol. Evol.* **24**, 1586–1591 (2007).

Acknowledgments: We thank J. Wilhelm and N. Stuurman for support in TIRF imaging; E. Griffis and P. Guo at the Nikon Imaging Center of UCSD for technical assistance in confocal imaging; P. Ordoukhanian at the Biophysics and Biochemistry Core of Scripps for performing BLI measurement; R. Ahmed and A. Sharpe for *Pdcd1*$^{-/-}$ mice; K. Jepsen at the IGM Genomics Center of UCSD and L. Wang for technical assistance in scRNA-seq; A. Kamphorst, T. Wu, and Y. Chen for technical advice; A. Y. Rudensky, Y. Liu, and J. Chen for discussions; and I. Mellman and members of the Hui laboratory for critically reading the manuscript. Microscopy and image analyses were performed at the Nikon Imaging Center or the Hui laboratory at UCSD. **Funding:** T.M. was supported by a postdoctoral fellowship from the Human Frontiers Science Program Long-Term Fellowship and JST PRESTO grant (JPMJPR22EB). This work was supported by National Institute of Health grants R37 CA239072 (to E.H.), R01AG074273 (to X.C.), and R01AG078185 (to X.C.); American Cancer Society grants AWD103481 and CAT-24-1374685-01-CAT (to E.H.); a Searle Scholar Award from the Kinship Foundation (to E.H.); and a Pew Biomedical Scholar Award from the Pew Charitable Trusts (to E.H.). J.D.B. was supported in part by the Hartwell Foundation. This manuscript includes data generated at the UC San Diego IGM Genomics Center using an Illumina NovaSeq X Plus that was purchased with funding from a National Institutes of Health SIG grant (no. S10 OD026929). **Author contributions:** T.M., J.D.B., and E.H. designed the project and wrote the manuscript. J.D.B., G.P.M., N.M., and S.M.H. designed the adoptive transfer experiment. N.M. and S.M.H. established the retrovirus system to simultaneously delete endoPD-1 via CRISPR and reconstitute exoPD-1 in mouse primary T cells. G.A.W. cloned constructs for Figs. 4 and 5 and structural representation of Shp2. L.C., C.W., and Z.Z. designed and conducted sequence evolution analyses and computational reconstruction of ancestral sequences. J.D.B., T.M., N.M., C.C., and Y.Z. conducted in vivo experiments. J.Z. prepared human primary T cells expressing PD-1 variants. T.M. performed all the other experiments and data analyses. E.H., J.D.B, L.-F.L., and X.C. obtained funding and supervised the project. **Competing interests:** E.H. consults for Tentarix Biotherapeutics. J.D.B. consults for Valora and DrKumo and serves as Chief Scientific Officer for Paramita Therapeutics and Pathfinder. All other authors declare that they have no competing interests. **Data and materials availability:** scRNA-seq data have been deposited to GEO (GSE280853). Tabulated data underlying the figures are provided in data file S1. Code used for the evolutionary analyses is located in GitHub (https://github.com/usernameCL311/PD1_evolution_analyses). All data needed to evaluate the conclusions in the paper are present in the paper or the Supplementary Materials (data file S1). Requests for materials should be addressed to E.H.

Submitted 21 August 2024
Accepted 4 December 2024
Published 3 January 2025
10.1126/sciimmunol.ads6295